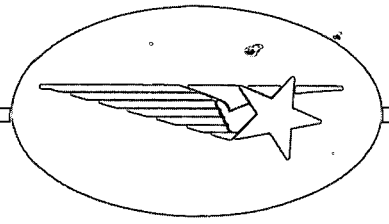

(NASA-CR-122510) MICROPHONE DENSITY GAGE EXPERIMENT FOR OGO-F Final Report (Lockheed Missiles and Space Co.) Jul. 1972 87 p CSCL 14B

N72-28467

Unclas

G3/14 36546

Lockheed

MISSILES & SPACE COMPANY

A GROUP DIVISION OF LOCKHEED AIRCRAFT CORPORATION

SUNNYVALE, CALIFORNIA

FINAL REPORT
FOR
MICROPHONE DENSITY
GAGE EXPERIMENT
FOR OGO-F

Contract No: NAS5-9334

July 1972

PREPARED BY

LOCKHEED PALO ALTO RESEARCH LABORATORIES
3251 Hanover Street
Palo Alto, California

for

GODDARD SPACE FLIGHT CENTER

GREENBELT, MARYLAND

SUMMARY

The Microphone Density Gage experiment was designed to make in situ measurements of the atmospheric density around much of the OGO-6 orbit. From this it would be possible to study atmospheric density variations which result from latitude changes, local time changes, and solar-activity related changes. The operating principle of this instrument lies in the transfer of momentum from the ambient neutral gas atoms and molecules, created by the relative velocity between the gas and the instrument, to the sensing element of the device, a thin metallic ribbon suspended between the pole pieces of a permanent magnet to form a microphone. Unfortunately, in flight a negative going zero shift appeared in the instrument output that had the effect of seriously reducing the effective sensitivity available. This made the resultant analysis more difficult to perform and, at the same time, made it impossible to meet in depth all of the experiment objectives.

Contained within this report is a description of the fabrication, installation and operation of the Microphone Density Gage instrument. An analysis of the resulting problems and minor failures is also given. The approach to the data analysis is discussed and the significant results obtained are given.

In spite of the difficulties, it has been possible to study 34 persistent density peaks (maximums) measured near 400 km during daytime (1425 LT) between geomagnetic latitudes 50°N and 61°N for a period approximately one and one-half days before and after an observation of a stable auroral red (SAR) arc by R. W. Owen at 0915 UT on July 14, 1969, near Richland, Washington. Most of the density peaks occured at geomagnetic latitudes, L values, and altitude characteristic of SAR arcs. The evidence is strong that these peaks result from the same energy transfer mechanism that causes SAR arcs. The average density change in the peaks was 27 percent.

Most of the 34 peaks appeared in the longitude sector from 150°E to 350°E. No density peaks were measured in the 50°E to 130°E sector during the three and one-half day observation period. A persistent pair of density peaks were present on 7 successive orbits during July 13 and July 14 (both geomagnetically-disturbed days) near geomagnetic latitudes 53°N and 61°N, respectively. These may be associated with a multiple SAR arc. Assuming that the density peaks are due to heating accompanying SAR arcs near 400 km, the average SAR arc occurring during the data period is estimated to be 500 Rayleighs and the average temperature change in the peaks is estimated to be 25°K. These results support Cole's thermal conduction model of the SAR arc.

Neutral density data obtained near 400 km (1600 LT) from 0° to 40°N geomagnetic latitude for 25 September through 3 October 1969 were studied. Several geomagnetic storms occurred during this period (a_p varied from 0 to 207). Least-squares fits were made to data points on density - a_p and density - D_{st} scatter diagrams, where the density values selected were delayed in time behind a_p and D_{st}. An equation representing the least-squares fit was computed for each delay time. The equation of best fit (and the corresponding time delay between the density and the magnetic index which resulted in this best fit) was found by choosing the equation that gave the minimum standard error. For example, the best fit at 10°N geomagnetic latitude occured for a_p at t-3 hr, where t is the time of the density values.

TABLE OF CONTENTS

LIST OF ILLUSTRATIONS

LIST OF ILLUSTRATIONS (Continued)

LIST OF ILLUSTRATIONS (Continued)

Chapter 1

INTRODUCTION

Chapter 1

INTRODUCTION

1.1 Introduction

The Microphone Density Gage is an instrument designed to measure in situ the spatial and temporal variations in the neutral atmospheric density around the OGO-6 orbit. It was specifically planned to measure (1) latitude variations, (2) day-night variations, and (3) solar activity-correlated variations in the atmospheric density.

The operating principle of this instrument lies in the transfer of momentum from the ambient neutral gas atoms and molecules, created by the relative velocity between the gas and the instrument, to the sensing element of the device, a thin metallic ribbon. The ribbon, suspended between the pole pieces of a permanent magnet to form a microphone, is mounted in the orbital-plane experimental package (OPEP) of OGO-6 looking along the velocity vector of the vehicle. The atmospheric gas, having effectively the velocity of the vehicle, exerts a pressure P on this ribbon equal to $k \rho v^2$, where k is a constant determined by the accommodation coefficient (taken to be = 1) and ρ is the atmospheric density. Since the satellite velocity is independently known, the pressure is a direct measure of the density. The gas striking the ribbon is mechanically chopped by a tuning-fork chopper which interrupts the gas flow at regular intervals to produce an oscillation of the ribbon in the magnetic field of a permanent magnet, the amplitude of which is proportional to the applied pressure. The electrical voltage generated by this ribbon motion through the magnetic field is amplified and rectified to provide a dc signal suitable for telemetry. In-flight calibration is provided to determine if the ribbon/electronics sensitivities have changed. The design of the instrument provided for an instrument sensitivity so that pressures equivalent to solar radiation pressure in free space could be detected by

the instrument. However, as shall be described later, a problem developed with the instrument which significantly reduced its pressure sensitivity.

In this report we shall describe the instrument, its fabrication and installation in Chapter 2. In Chapter 3 the acquisition of data will be discussed, emphasizing the approach to the analysis and the computer programs developed to handle the work. The results obtained are discussed in Chapter 4.

Chapter 2

THE RMDG INSTRUMENT

Chapter 2

THE RMDG INSTRUMENT

2.1 Instrument Description

The general philosophy of operation of this device was given in the preceding section. The details of operation will be given here. Figure 2-1 is a block diagram of the Ribbon Microphone Density Gage (RMDG) as it has been designed for the OGO-F program. The entrance slit for this instrument is assumed to be the lower left hand corner of the figure where a particle (neutral gas) stream is shown moving from left to right. The particle beam actually contains ions and electrons as well as neutral gas molecules and atoms, and these charged particles are deflected from the ribbon by the transverse electric field between the grounded "shutter" and the negative "ion getter". The neutral stream passes through the mechanical chopper, which is a "tuning fork" chopper, and this chopped beam strikes the sensing element, the metallic ribbon. This interrupted gas stream causes the ribbon to execute a forced oscillation at the chopping frequency which, since the ribbon has a strong magnetic field normal to its length and also to the gas direction, creates an alternating electric voltage across the ends of the ribbon.

The alternating voltage thus created is transformer coupled into a preamplifier as shown in the figure. The voltage gain of the transformer is about 70 and of the preamplifier is about 3×10^3 for the frequency of the signal obtained, giving a total a-c gain of about 2.1×10^5 for this part of the system. The extreme sensitivity of the sensor and electronics requires that the ribbon microphone, transformer and preamplifier be carefully shielded and mechanically decoupled from the body of the instrument by suspending them on a set of weak springs so that in the gravity-free environment of the orbit the ribbon will be centered properly on the entrance slit of the instrument.

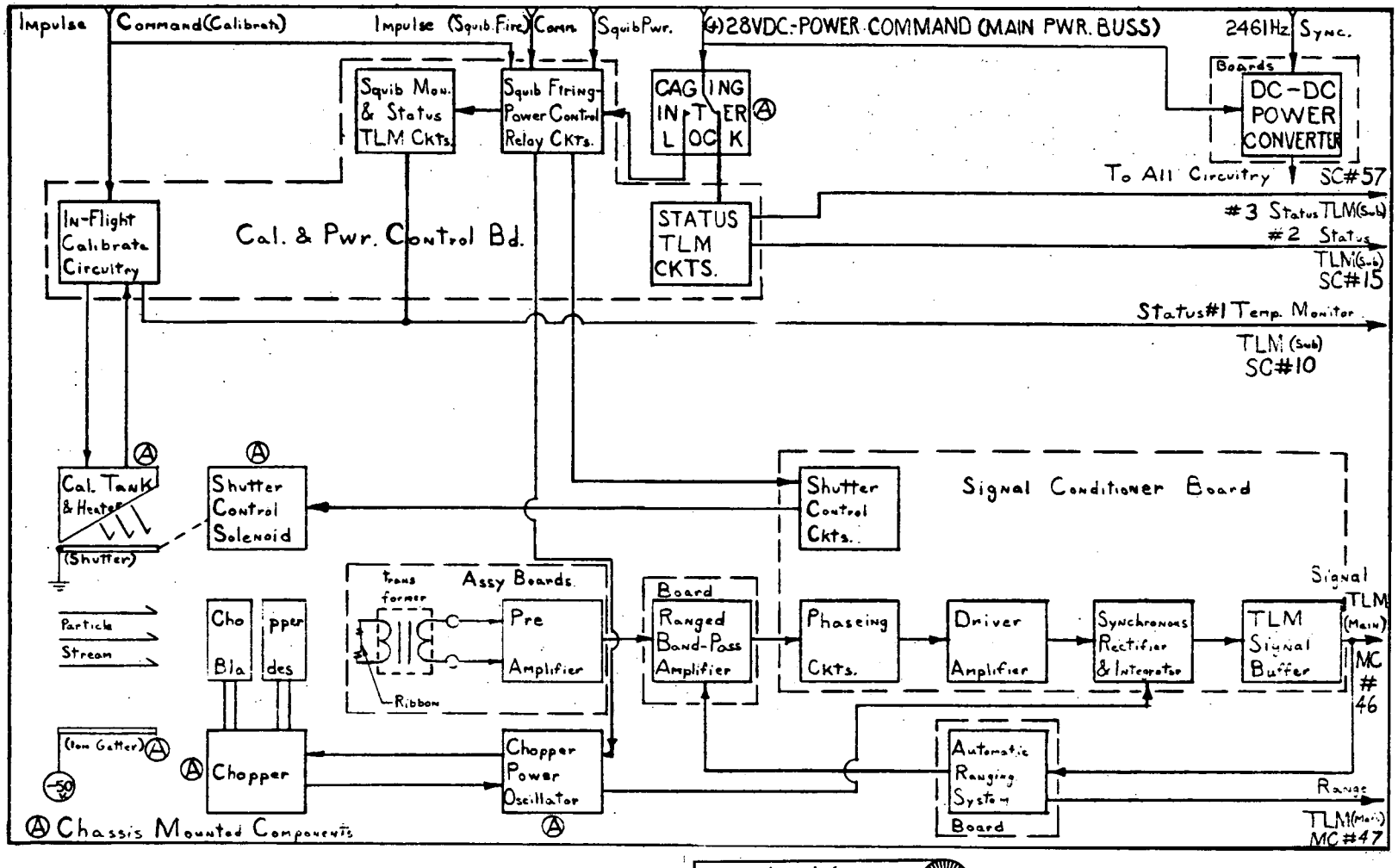

Fig. 2-1 Experiment Block Diagram

The signal from the preamplifier is fed into an automatic ranged band-pass amplifier which has four ranges of voltage amplification. The gains of this amplifier are 686, 98, 14 and 2, the selection of the gain is determined from the voltage output of the instrument. The signal from the ranged amplifier passes through a circuit designed to adjust its phase properly, then into a driver amplifier which makes the signal suitable for a synchronous rectifier and integrater. The synchronous rectifier is driven by a signal from the chopper power oscillator so that it is in phase with the signal. The phasing circuit is used to compensate for any natural phase shifts in the rest of the circuitry. As shown in Figure 2-1, the rectified and integrated signal output is made acceptable for the telemetry by a telemetry signal buffer circuit, and the output of this is utilized to select the range to be used in the ranged amplifier. The range in use is indicated by the automatic ranging system and appears as an additional output for the instrument.

Since the output of this instrument will be a relatively slowly varying voltage there is some necessity to verify the instrument "zero" level in the output. This is done with the shutter shown at the entrance slit of the instrument on the left side of Figure 2-1. This mechanical shutter, which forms the ground plane of the charged particle deflection field, is closed periodically by the shutter control solenoid and the incoming gas stream cannot exert a pressure on the microphone ribbon. The shutter control circuit is free-running and activates the solenoid approximately once every 2 minutes, holding the shutter closed for about 20 seconds each time.

An in-flight calibration of the total sensor/electronics system is also provided. The in-flight calibration source is a thermally insulated tank containing anthracene crystals, resistance heaters and a thermistor, all of which is mounted behind the shutter as shown on the left side of Figure 2-1. This tank is sealed except for a small

hole on one face located so as to have a clear view of the ribbon through the chopper blades when the shutter is activated and to be covered by an insulating material on the back of the shutter when the shutter is open. Upon command, power is supplied to the in-flight calibrate circuitry which, in turn, applies power to the heaters in the tank and activates a thermal control circuit which uses the thermistor in the tank as a sensor. In approximately one-half hour the calibration tank and anthracene are at their operating temperature, which is approximately 85°C. At this temperature the anthracene crystals have a vapor pressure of sufficient magnitude that a gas stream effuses from the small hole in the tank (when the shutter is activated) and impinges upon the ribbon with a pressure suitable for measurement. This gas stream is chopped, just as is the incoming gas stream when the shutter is open, and so a calibration signal is generated that can be used for in-flight comparison to ground-based measurements. This in-flight calibration scheme does not interfere with the regular taking of data, but replaces the background "zero" measurements when commanded to operate. It was intended that this command would be exercised for a full orbit at a time and probably no more frequently than once every week.

The ribbon microphone, transformer, and preamplifier are contained as a unit in a metal can and this can is mounted on a set of 8 opposing springs which serve to keep this can suspended and free from direct mechanical connection to the rest of the system while in the gravity-free environment of orbital flight. During the powered phase of this mission (i.e., during launch and orbit injection) this "free floating" can must be locked securely so as to prevent damage to the components. A plunger-bumper system accomplishes this hold down and the plunger is released by firing a squib mechanism upon ground command. The command inputs and block representation for this squib firing operating are shown in upper center of Figure 2-1. Associated with this are squib monitor and status circuits.

When the inner can is caged there are provided power interlocks which make it so that power cannot be applied to the shutter control circuits or to the chopper power oscillator. This prevents damage to the system when the instrument is turned on. Also the shutter is mechanically restrained when the inner can is caged to prevent damage to it. The circuitry for these are represented in the top part of Figure 2-1. Also shown in this figure are the power converter, the 2461 Hz sync input, and the three sub-com status words used to monitor the status of the various things described above.

2.2 Mechanical Details

The physical dimensions and mechanical details of this instrument are best described by referring to the Installation Control Drawing, a reproduction of which is shown as Figure 2-2. As seen in the figure this instrument has the basic shape of a rectangular box whose base plate is 7.457 inches by 6.110 inches and whose height is 6.125 inches. The instrument was mounted in OPEP No. 1 with the designated mounting surface attached directly to the OPEP base plate so that the instrument face containing the rectangular sensor opening and squib mechanism was against the forward-looking face of the OPEP. This OPEP face had cut-outs to allow for the sensor opening and the squib extrusion.

The side view (left hand figure) of the instrument shows the required view angle for the instrument ($\pm$ 45°), the squib power plug attached to the squib, and a service hole through which the instrument may be recaged should it become uncaged during testing. This instrument was mounted in the center of the OPEP between two other experiments. Therefore, direct access to the power plugs originally installed on the instrument was not possible. The electrical interface with the instrument was accomplished by bringing cables directly out of the instrument and over to the side wall of the OPEP where they were attached to the OPEP wall. A view of this cabling arrangement is shown in the top view (top figure) of Figure 2-2. The detail of the plug mounting

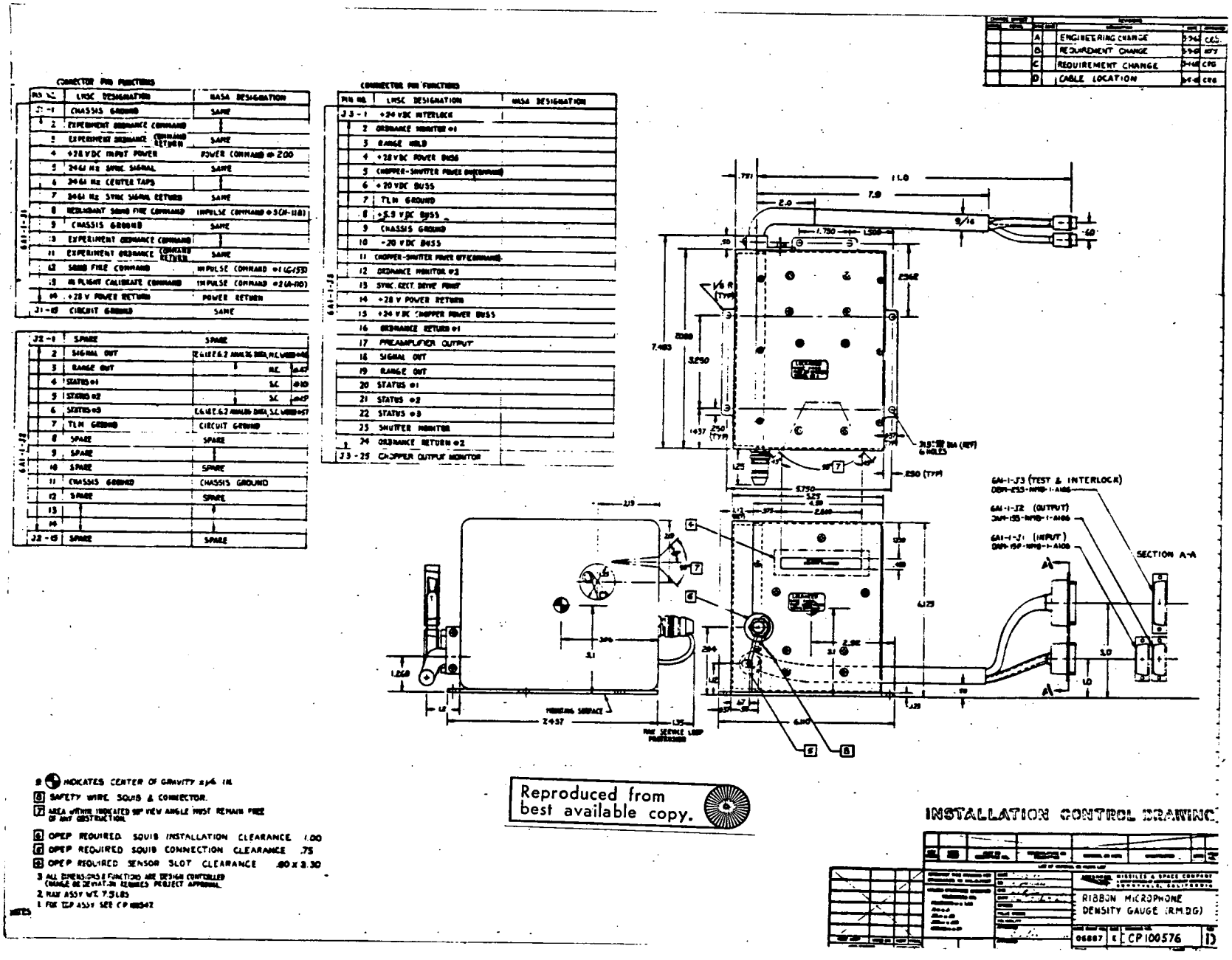

Fig. 2-2 Experiment Installation Control Drawing

to the OPEP wall is shown in Section A-A. The base plate with its mounting hole pattern is shown in the top view of the figure. The irregular shape of this base plate accommodates the base plates of the adjacent packages.

Also shown in Figure 2-2 are the pin connections for each of the electrical plugs and the location of the instrument center of gravity. The center of gravity designations are seen on the left view and the front view of the instrument. The base plate of the instrument is gold plated aluminum to provide good electrical and thermal contact with the OPEP. The instrument box is also aluminum but is painted with a black epoxy paint for thermal control.

2.3 Electrical Details

The electrical interface of this instrument with the vehicle is accomplished through two plugs, 6A1-1-J1 and 6A1-1-J2 (seen as J1 and J2 in Figure 2-2). Plug J1 contains all of the inputs from the spacecraft to the experiment, i.e., Primary Power, Ordnance Power, Ordnance Fire Commands, In-Flight Calibrate Command, the appropriate grounds and power returns. Plug J2 contains all of the outputs from the experiment to the spacecraft. As can be seen from the J2 plug listing in Figure 2-2, the signal out of the instrument is connected to Main Com Word No. 46 and the range indicator for the amplifier is connected to Main Com Word No. 47. The essential features of the data are given by these two analog outputs. The voltage seen on Word No. 46 may be any value between 0 and 5 Vdc. The range output, Word No. 47, will be at one of four distinct voltage levels depending upon the range of the amplifier. Range 1, the highest gain position of the amplifier, is indicated by an output voltage of 1.4 ± 0.1 Vdc; Range 2 by 2.5 ± 0.1 Vdc; Range 3 by 3.35 ± 0.1 Vdc; and Range 4 by 4.0 ± 0.1 Vdc.

The three subcom analog words used to monitor the status of this instrument are Subcom Words No. 10, 15 and 57. Subcom Word No. 10,

called Status No. 1, monitors the application of squib power and the operating of the in-flight calibration system. The output of this word normally reads zero volts dc. When squib power is applied it will read 1 $\pm$ 0.3 volts dc. Upon application of the in-flight calibrate command, Impulse Command #110A, if the instrument is powered at the time, the signal output will jump to 4.5 $\pm$ 0.5 Vdc and will slowly decrease with time until it stablizes at 1.5 $\pm$ 0.2 Vdc and will remain at that level until either the power is removed from the instrument or the IFC Command (#110A) is given again at which time it will return to zero.

Subcom Word No. 15, called Status No. 2, monitors the +28V bus power applied to the instrument. It was the word used to indicate whether or not the instrument was powered. With the instrument in its caged configuration this word will read 3.0 $\pm$ 0.2 Vdc for approximately 2 minutes and then drop to 2.4 $\pm$ 0.2 Vdc for about 20 seconds the cycle being repetitious. In flight, with the instrument powered before being uncaged, the voltage would read 3.6 $\pm$ 0.2 Vdc for approximately 2 minutes and 3.0 $\pm$ 0.2 Vdc for about 20 seconds. Again, in flight, the instrument could have been powered, uncaged and the shutter inoperative under which circumstances the voltage would read 2.4 $\pm$ 0.2 Vdc for 2 minutes and 1.1 $\pm$ 0.2 Vdc for 20 seconds. The expected normal flight operation was the instrument powered, uncaged and with both shutter and chopper powered. The output of this word would then read 3.3 $\pm$ 0.2 Vdc for a $\neq$ 28 Vdc power bus and there should be no observable "notch" in this voltage reading.

Subcom Word No. 57, called Status No. 3, was used to monitor the various voltages generated by the instrument's power converter. These converter voltages are mixed to give this output. For the instrument powered and caged the output voltage for Word No. 57 will be 2.4 $\pm$ 0.3 Vdc for approximately 2 minutes and 0.6 $\pm$ 0.2 Vdc for about 20 seconds, the cycle being repetitive. For an uncaged configuration with chopper and shutter off the voltages are the same as the caged values. For

the instrument uncaged with the chopper and shutter also powered, i.e., in the normal flight operating condition, the voltage output would be 2.3 $\pm$ 0.3 Vdc for about 2 minutes and 1.4 $\pm$ 0.3 Vdc for 20 seconds repeating.

2.4 Power Requirements

The power consumption of this instrument was not uniform due to the periodic shutter operation and the commanded in-flight calibration sequence. Figure 2-3 is a diagram of the current drawn from the power bus as a function of time for normal and in-flight calibration operation. The magnitude of the current drain is dependent upon the bus voltage, so the values shown in the figure are for a 28 Vdc power bus. The time is plotted on a logarithmic scale to permit both detailed and expanded views of the power profile. As shown in the figure the solid lines describe the data mode, or normal mode, of operation. For 100 seconds the current drawn is 190 ma and for 20 seconds, while the shutter is activated, the current drawn is about 500 ma. This pattern is repeated until power is removed or the In-Flight Calibration sequence is initiated. During In-Flight Calibration Mode the instrument draws 345 ma for 100 seconds and then 665 ma for 20 seconds. This repeats for approximately 30 minutes at which time the power is slowly reduced so that the current drain becomes 285 ma for 100 seconds and 590 ma for 20 seconds. The power consumption remains at this level until the instrument is taken out of the IFC Mode. The following summarizes the power consumption at 28 Vdc bus voltage for easy reference.

Minimum Power	5.3 watts
Maximum Normal Power	14.3 watts
Maximum IFC Power	18.6 watts
Maximum Average Power	11.04 watts
Normal Average Power	6.65 watts

2.5 Thermal Characteristics

The following summarizes the temperature limits for this experiment.

Safe Operation	-10°C to + 50°C
Satisfactory Data	-10°C to + 50°C
Safe Storage (Non-Operating)	-37°C to + 70°C
Minimum Turn-on without permanent damage	-37°C

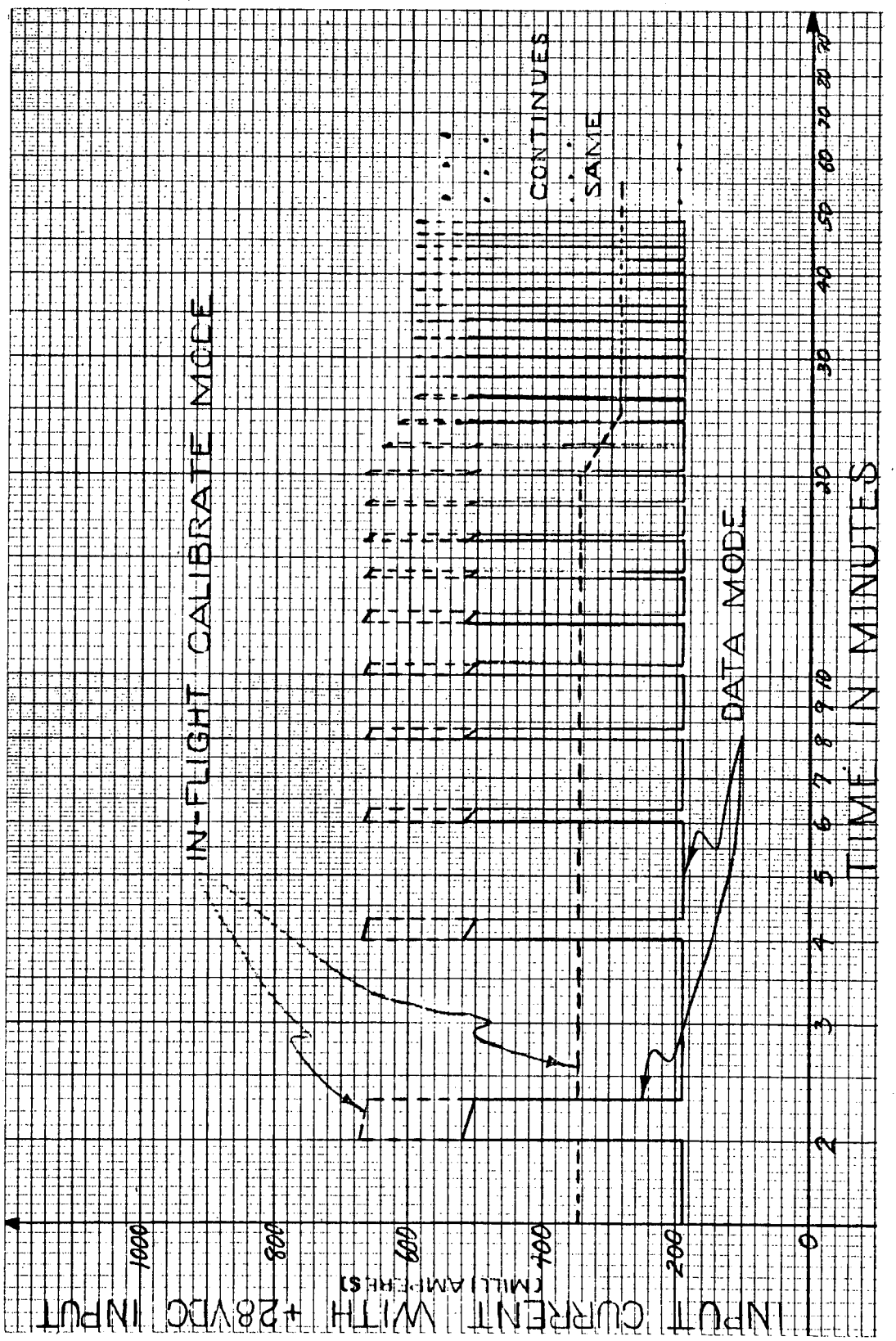

Fig. 2-3 Experiment Power Profile

Although it is indicated by the above that the Safe Operation and Satisfactory Data regions are the same, it may be possible to turn this instrument on at temperatures as low as -37°C without causing any permanent damage. At very low temperatures what could happen when power is applied to the instrument is that the power converter might fail to begin to oscillate. Should this happen permanent damage would result to the converter unless the instrument power is removed rather quickly (in a few minutes). The indication that the converter is not operating is that Subcom Word No. 57 reads 0.0 ± 0.2 Vdc while Subcom Word No. 15 reads $+3.3 \pm 0.4$ Vdc. In actual fact there is no real lower limit to the storage temperature for this instrument although it must always be remembered that the instrument temperature must be raised to at least -37°C before it is turned on.

2.6 Ordnance Description

The ordnance device utilized in Experiment F-01, Ribbon Microphone Density Gage, actuates, or extends, a captive piston which rotates a locking arm to release the plunger holding the "floating" inner can mechanism rigid against rubber stoppers. All parts of the mechanism, though spring-loaded, are captive and cannot be ejected from the instrument. All of this takes place behind a cover over the instrument. There is a relocking access hole through this cover, however, and if someone had their finger in this hole at the time a squib is fired, they could be injured by the rapid motion of these various mechanical parts.

The ordnance device was a Holex R 6299A Actuator and had the following characteristics:

No-Fire Current	1.0 amp max for 5 minutes
All Fire Current	4.5 amp
Bridgewire Resistance	1.0 ± 0.1 ohm
Pin-to-Case Resistance	2 megohms min.
Pin-to-Case No-Fire Voltage	500 volts ac RMS max.

The ordnance was not installed until the spacecraft was on the pad at the Western Test Range. From the safety point of view the bridge

was shorted out through relay contacts whenever the device was plugged into the instrument, as can be seen from the schematic shown in Figure 2-4. An additional shorting was provided through a Red Tag plug cover so that the squib could not be accidentally prefired.

2.7 Flight Operation

As described in a previous section the Ribbon Microphone Density Gage (RMDG) was mounted in the OPEP ready for flight in a clamped configuration so that the powered phase of the flight would not cause any damage to the operationally "floating" sensor can. After the spacecraft was in orbit and the OPEP was erected and activated, power was applied to the RMDG. Power is applied by the application of Power Command 200/220. At this time the squib was fired to release the sensor can and allow it to achieve its equilibrium position under the action of the eight opposing springs. The squib is fired by applying ordnance power and then impulse command No. 153 Relay Group G to the instrument. This squib firing also closed two parallel interlock switches which permited power to be applied to the shutter solenoid. In this configuration the instrument was ready to collect data.

After the squib has been fired the only spacecraft input required to operate this instrument is the primary power supply. The instrument power converter does respond to the 2461 Hz sync signal, but is not dependent upon it. Successful data taking is dependent upon the OPEP operating properly; that is, so that its front face looks into the velocity vector. The operation of the shutter, described in the previous section, is controlled by a timing circuit contained within the experiment package. The shutter was closed for approximately 20 seconds every two minutes providing a background signal level to be compared to the signal being obtained from the atmospheric density.

Periodically, it was desired to obtain an in-flight calibration of the sensing system. This was done by applying the In-Flight Calibration Command (Impulse Command #110, Relay Group A) to the experiment. This command activated the heater and temperature control circuitry

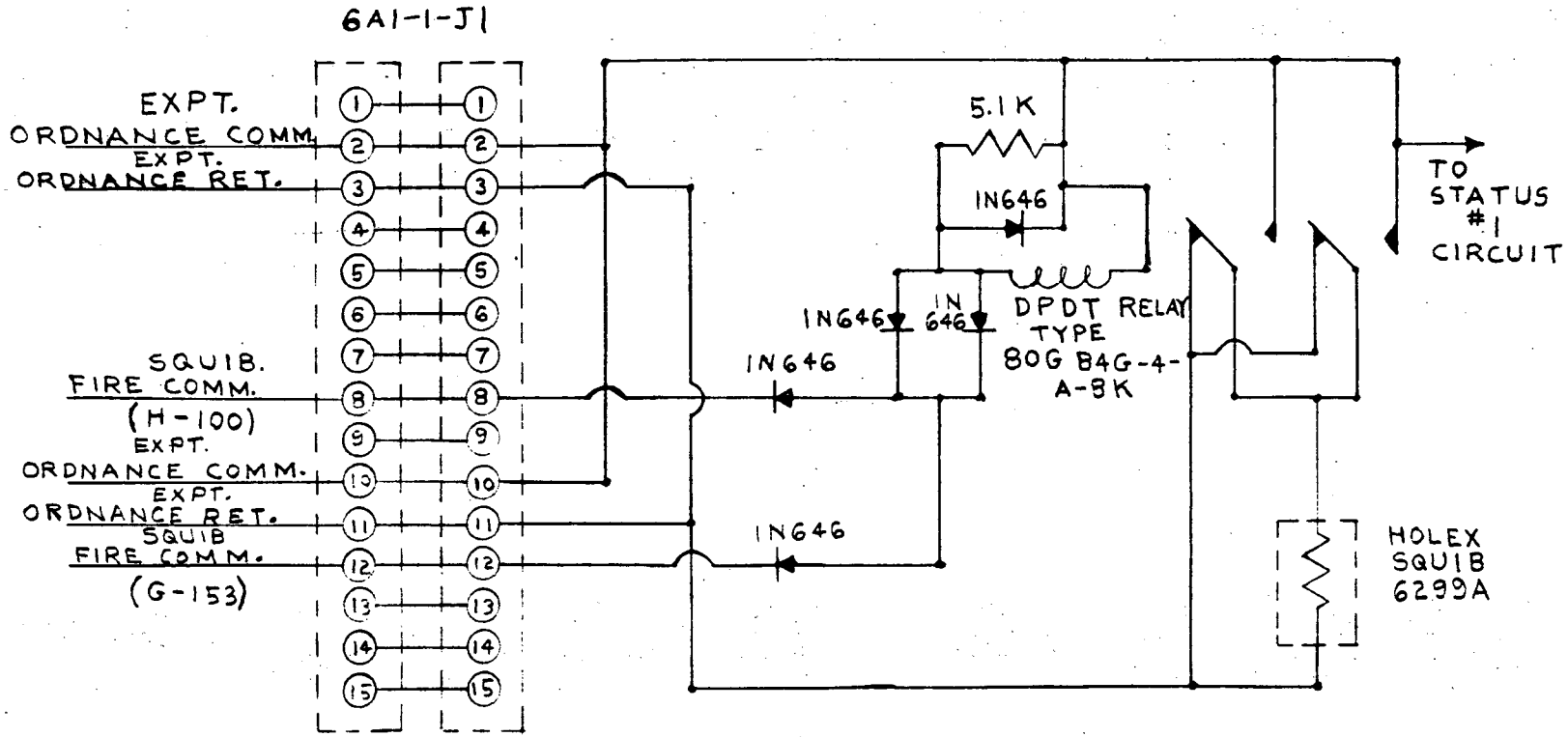

Fig. 2-4 Squib Circuitry and Interface Diagram

described previously. It required approximately thirty minutes for this to get up to temperature (a monitor for this was available on one of the instrument subcom words), so it was necessary to operate this in-flight calibration system for a complete orbit at a time. It was not desirable to operate it for longer than one orbit so care had to be taken to select a suitable orbit for the exercising of this in-flight calibration system. Density data was still obtained while the in-flight calibration system operated because the molecular stream coming from the IFC can was only exposed to the ribbon sensor when the shutter was activated (for about 20 seconds of each two minutes). The In-Flight Calibration system was turned off by re-application of the IFC Command, Impulse Command #110, Relay Group A..

The flight unit was integrated on the spacecraft and placed in orbit on June 5, 1969. The instrument was turned on about 25 hours later. At this time it appeared that the output signal was running negative which indicated a rather severe outgassing problem in the OPEP. However, since the instrument used phase-controlled ac signals to obtain its dc output, the observed output could have been a manifestation of circuit phase-change or out-of-phase noise injection.

The in-flight calibration was included to help sort out these types of problems. However, it was found to be very difficult to initiate the IFC operation from the appropriate command signals. Subsequent experience has shown that this difficulty lay more with the command system itself than the experiment. By exercising this IFC it was determined that the instrument itself was working and that the calibration was not appreciably different than was experienced in laboratory checkout and calibration.

With the passage of several days some signals were observed near vehicle perigee which were clearly from atmospheric density. The fact that these signals gradually appeared verified that there was a rather severe outgassing problem initially on OGO-6. The nature of

the observed signals have also suggested that the alignment of the OPEP, the alignment of the instrument on the OPEP, or the geometric arrangement of the shutter-chopper-sensor system was not optimum. It has not been possible to identify which one or ones of these may be having an effect on the signal, but it does seem that the sensor (ribbon) is not seeing the full gas stream as it should for accurate operation.

The instrument continued to operate in this manner, showing significant atmospheric density signals on nearly every perigee pass of the vehicle until about the second week in February, 1970. At this time there appeared to be a phase reversal of some kind in the circuitry which generally put the steady background signal reading several volts positive on range 3 of a four range system. Atmospheric density signals near and at perigee appear as decreasing positive signals from this background level. It is still possible to read the density signal from this configuration, but it confuses the initial calibration of the instrument. Application of the in-flight calibration signal (which became easy to do since a different command link was being used) has made it possible to make sense from these signals, but this phase-change does make the data analysis somewhat more difficult to perform.

The instrument continued to operate in this reversed-phase mode until the OGO-6 vehicle was turned off.

Chapter 3

DATA ANALYSIS

Chapter 3

DATA ANALYSIS

3.1 Data Calibration and Validity

In view of the problems noted in the previous chapter, a model atmosphere [Anderson and Francis, 1966] was used to calibrate the instrument readings near perige . The density measurements were selected from 20 orbits whose perigee latitudes were near the equator during two days with very low geomagnetic activity ($A_p = 2$): 19 July and 29 July 1969. First, the instrument readings were normalized to a constant altitude, local time and solar activity. Second, ratios of the model densities to the normalized readings were derived. These ratios ranged from 5.3 to 7.6, averaging 6.4. Third, the instrument readings were multiplied by 6.4 to derive the final density values.

Instrument readings from some orbits exhibited an oscillation in the data points with a period less than 30 seconds. The extreme sensitivity of the sensor and electronics required that the ribbon microphone, transformer, and preamplifier be carefully shielded and mechanically decoupled from the body of the instrument by suspending them on a set of springs so that in the gravity-free environment of the orbit the ribbon will be centered properly on the entrance slit of the instrument. Since the ribbon microphone is spring mounted, it can vibrate so that on occasion its orientation could be changing at a constant rate. In order to eliminate this oscillation, the maximum data point occurring in any 30-second interval was selected (from the nearly 210 data points taken in that interval) as the most representative one. This maximum value is most likely to occur when the ribbon's orientation is such that it is most nearly centered on the entrance slit of the instrument. Consequently, the final data points derived following the above procedure have an average time separation of one-half minute and an average distance separation of 2 to 3 degrees

in latitude.

To check the accuracy of the final density values derived above against independent data, two other experiment flown on OGO-6 were used for comparison. These were experiment F-04 (Reber) Quadrupole Neutral Particle Mass Spectrometer and Experiment F-14 (Blamont) 6300A Airglow Emission, which measured neutral composition and temperature, respectively. The mass spectrometer of Experiment F-04 [Reber et al., 1971] measured neutral specie number densities. Data from orbit 1640 and 1641 for 27 September 1969 were made available [C. A. Reber, private communication, 1971]. The total mass density can be expressed with little error as

$$\rho = n(O)\, m(O) + n(N_2)\, m(N_2) \qquad (3\text{-}1)$$

where $n(O)$ and $n(N_2)$ are the measured number densities of atomic oxygen and molecular nitrogen, respectively, and $m(O)$ and $m(N_2)$ are the masses of atomic oxygen and molecular nitrogen, respectively. The measurements indicated about 87 percent O, 12 percent N_2, and one percent He_4. The helium, therefore, was neglected in the calculations.

Figure 3-1 shows two curves of the mass density for orbit 1640 near the perigee altitude (398 km), where the solid curve connects density points derived from the microphone density gage data and the dashed curve connects points derived from the mass spectrometer data. The difference between the two curves ranges from 24 to 39 percent, with the microphone density gage curve averaging 31 percent lower. Figure 3-2 exhibits the same two curves for orbit 1641. The difference ranges from 16 to 26 percent, with the microphone density gage curve averaging 21 percent lower. Thus, the average difference between the two curves for both orbits is 26 percent. This amount of agreement is good considering the degree of variability of the atmosphere at 400 km, the uncertainties connected with the model atmosphere, the measurements with the microphone density gage, and the mass spectrometer. Errors in mass spectrometer measurements are estimated to be between 25 and

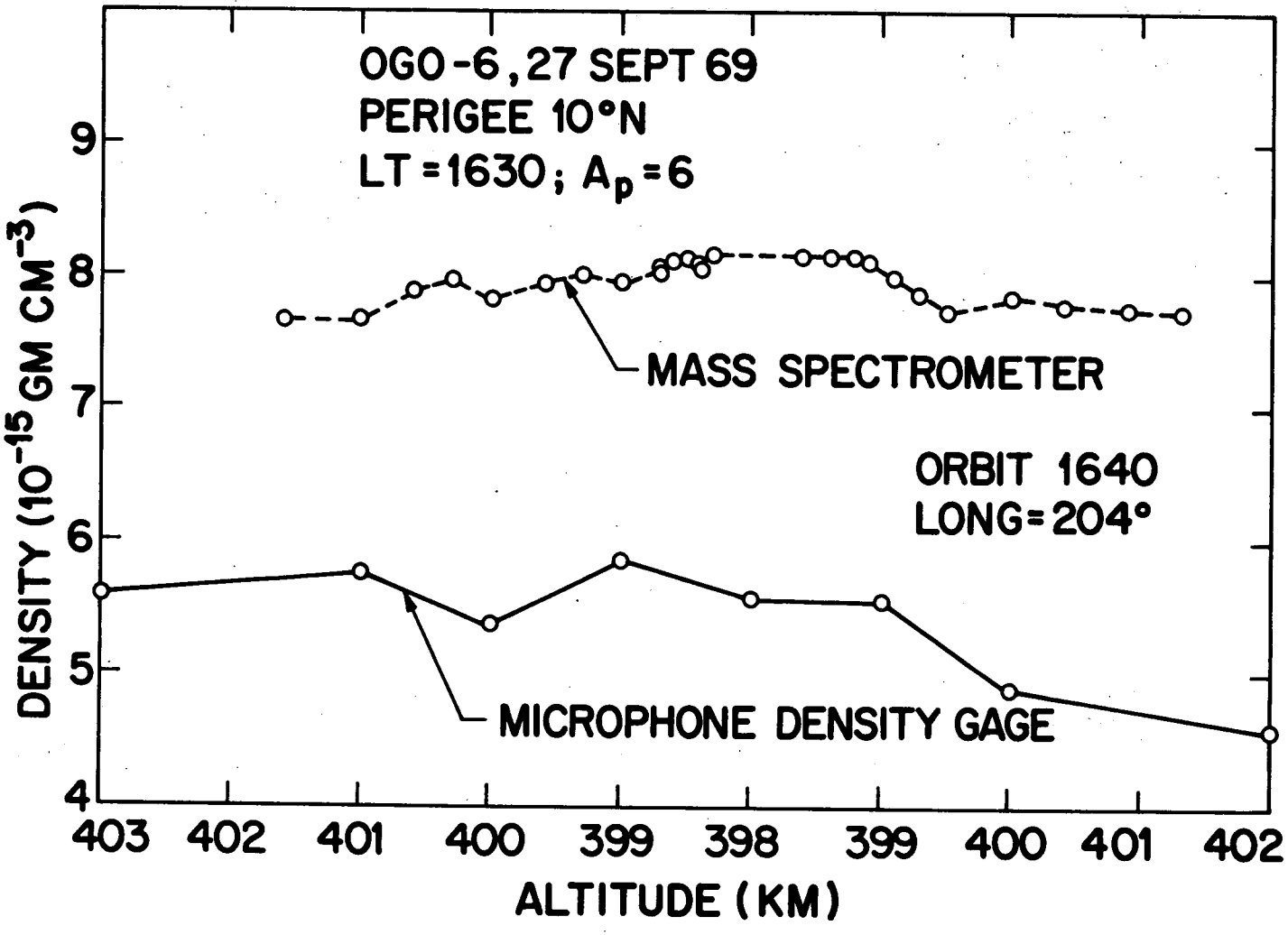

Fig. 3-1 Comparison of neutral density derived from OGO-6 Lockheed Microphone Gage with values from mass spectrometer (Reber et al, 1971) for orbit 1640, 27 September 1969.

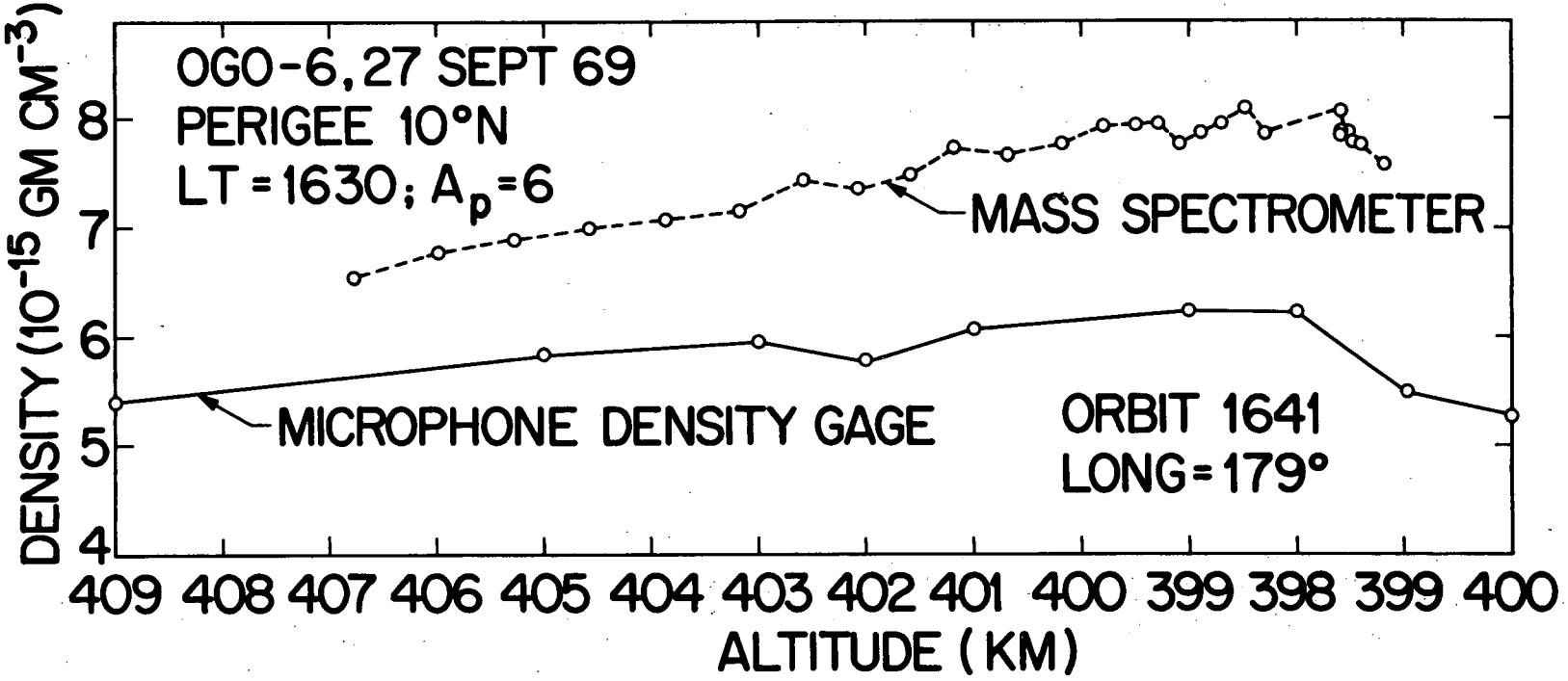

Fig. 3-2 Comparison of neutral density derived from OGO-6 Lockheed Microphone Gage with values from mass spectrometer (Reber et al, 1971) for orbit 1641, 27 September 1969.

50 percent [Nurre and DeVries, 1970].

Experiment F-14 contains a Fabry-Perot Interferometer [Blamont and Luton, 1970] which gives the profile of the 6300A oxygen line in the dayglow at different altitudes between 200 km and 350 km. The temperature of the neutral atmosphere can be deduced from the profile of the 6300A line. Blamont and Luton 1970 present maps of the temperature of the neutral atmosphere at an altitude of 260 km for 27 September 1969 and 28 September 1969 at approximately 1600 LT near the equator. Blamont and Luton's temperature data can be used to derive the exospheric temperature. For the same solar activity and local time, the atmosphere is isothermal above 340 km, and the exospheric temperature is about 10 percent higher than that at 260 km [Anderson and Francis, 1966]. Therefore, Blamont and Luton's temperatures were multiplied by 1.1 to derive the exospheric temperature. These temperatures could then be compared with exospheric temperatures derived from the microphone density gage data by means of Dalton's law.

$$T = m\,g\,h \,/\, k(\ln \rho_o - \ln \rho) \qquad (3\text{-}2)$$

where m is the mean molecular mass (2.90×10^{-23} g), g = 865 cm-sec^{-2}, h is the altitude above 398 km, k is the Boltzmann constant, ρ_o is the density at perigee and ρ is the density at altitude h. Using Equation 3-2 to calculate T for 25 perigee passes (average latitude 24°N) where h averaged 16 km, gave an average temperature of 1100°K. Blamont and Luton's corresponding average temperature was 1215°K. Hence, the temperature derived from the microphone density gage data averaged 9.5 percent lower than Blamont and Luton's corrected temperatures. Blamont and Luton (1970) state an accuracy of $\pm$ 50°K for their temperature.

A check on the accuracy with which the microphone density gage can measure relative density variations was made by determining the difference in density between successive orbits on 27 and 29 September 1969. Latitudinal density profiles at 406 km were derived for each orbit by fitting smooth curves to normalized density gage values. The density was selected from each profile at seven locations at five-degree

intervals from 0 to 30°N. Then the difference in the density at the same latitudes was computed for adjacent orbits. The average density difference for 27 September 1969 was 7.8 percent (based on 14 orbits); it was 9.7 percent (13 orbits) on 29 September 1969. The larger difference on 29 September, a geomagnetically-disturbed day (A_p = 71), is probably due to an increased density variation between successive orbits because of heating changes associated with geomagnetic perturbations. On this date the average density between 0 and 30°N was 38 percent higher than 27 September, an undisturbed day (A_p = 6). Some of the major density differences between successive orbits (20 to 40 percent) were due to peaks appearing in the latitudinal density profile, averaging several degrees in width, which changed latitude from orbit to orbit. Also some of the density differences are undoubtedly due to differences in longitude [DeVries et al., 1966]. Inasmuch as the above factors are real, it appears likely that the microphone density gage can measure the relative density variation with an error less than five percent.

3.2 Analysis Approach

In analyzing the data obtained from the Microphone Density Gage only two main com words entered directly into the computation for density, the signal and range outputs (refer to the previous chapter). Each of these words was sampled once each main frame sampling. Thus at the 64 k bit data rate each word was read about 55 times per second, at the 16 k bit rate about 14 times per second, and at the 8 k bit rate about 7 times per second. Virtually all of the data we analyzed was taken at the 8 k bit rate (tape recorder dumps).

The instrument was calibrated in the laboratory by operating it in a vacuum chamber properly located a known distance behind a hole in a pressure chamber. The hole size, distance from source to instrument, and source gas pressure range were all selected so that gas molecules from the source could impinge upon the ribbon microphone by the process of molecular effusion, or free molecular flow, thereby permitting an accurate computation of the pressure experienced by the ribbon. Thus, the computational procedure necessarily refers to the

gas pressure in the source chamber. The relationship between the pressure experienced by the ribbon and the gas pressure in the source for the geometry used in this calibration is

$$P_r = 7.1 \times 10^{-4} P_s \qquad (3\text{-}3)$$

where P_r is the pressure on the ribbon in dynes/cm^2 and P_s is the gas pressure in the source in microns. Within the constraint of requiring that the source pressure remain low enough to maintain a condition of free molecular flow the relationship in (3-3) remains linear. Thus P_s can be replaced by $p_s \times S$, where p_s is the calibration factor in microns pressure per volt of output signal and S is the output signal in volts.

In flight operation the pressure exerted on the ribbon by the neutral gas can be given by

$$P_r = k\rho (V \cos \theta)^2 \qquad (3\text{-}4)$$

where ρ is the neutral gas density in gm/cm^3, V is the relative velocity between the spacecraft and the ambient gas in cm/sec, θ is the angle between the normal of the ribbon surface and the vehicle velocity vector, and k is a constant whose value depends upon the accommodation coefficient of the gas atoms and molecules striking the ribbon. For convenience, k is taken to be 1.0, which assumes the gas strikes the surface and accomodates to the ribbon temperature. For the extreme opposite condition, specular reflection, k would only be 1.3 so no serious error is made by taking k = 1. Making this assumption and putting (3-3) and (3-4) together we obtain for a final computational equation

$$\rho = 7.1 \times 10^{-4} S\, p_s (V \cos\theta)^{-2} \qquad (3\text{-}5)$$

In practice the velocity vector factor, $V \cos\theta$, was obtained by taking the vector dot product of the vehicle velocity vector and the actual OPEP roll axis vector as given on the orbit-atitude mag netic tapes. Since this was an automatic ranged instrument the calibration factor p_s was different for each range. These factors are given below

Range	p_s (microns/volt)
1	0.1
2	0.7
3	3.5
4	18.0

As was mentioned previously the instrument experienced an anomalous negative-going zero shift in orbit. This had to be accounted for in the value of S used in (3-5). Also, as pointed out in Section 3.1 comparison to atmospheric models indicated the need to correct the measured density values by a factor of 6.4. Thus the "S" used in (3-5) assumes the following form.

$$S = (\text{Signal output} - \text{Signal Zero}) \times 6.4 \quad (3\text{-}6)$$

The signal output is the actual voltage reading from the telemetry signal out and the Signal Zero is different for the range of the instrument amplifier. These Signal Zero values are:

Range	Signal Zero (volts)
1	-5.6
2	-0.2
3	0.0
4	0.0

This, then, outlines the procedure that was followed in converting the raw data as received on magnetic tape to atmospheric density values. The majority of the data processed has been from the on-board tape recorder taken at the 8 k bit rate. For this data each data point was processed to give a density value. To eliminate what appeared to be random oscillations of the data (presumably from motion of the "floating" inner can) the maximum density value in a 30 second time interval was selected and plotted as being representative of the data in that interval. The final data analysis was performed from plots of this kind of 30 second interval data.

3.3 References

Anderson, A. D., and W. E. Francis, The Variation of the neutral atmospheric properties with local time and solar activity from 100 to 10,000 km, J. Atmospheric Sci., 23, 110, 1966.

Blamont, J. E., and J. M. Luton, OGO-VI direct measurements and monitoring of the temperature of the neutral atmosphere from 200 to 350 km of altitude: the magnetic storm of Sept-Oct 1969, Centre National de la Recherche Scientifique Rept. f.18, 1970.

DeVries, L. L., E. W. Friday and L. C. Jones, Analysis of density data from low-altitude, high-resolution satellite tracking data, Southern Illinois University Tech. Rept. 188 (N 67-23490), 1966.

Nurre, G. S., and L. L. DeVries, An experiment to determine density variations in the earth's atmosphere and other atmospheric and aerodynamic information, Fourth National Conference on Aerospace Meteorology, May 4-7, 1970, Las Vegas, Nevada.

Reber, C. A., D. N. Harpold, R. Horowitz and A. E. Hedin, Horizontal distribution of helium in the earth's upper atmosphere, J. Geophys. Res., 76, 1845, 1971.

Chapter 4

RESULTS

Chapter 4

RESULTS

4.1 Geomagnetically Aligned Neutral Density Peaks

The period 12-15 July 1969 was selected for detailed analysis because of an unusual pair of density maximums that occurred at nearly fixed latitudes for seven successive orbits near the middle of this period. Figure 4-1 illustrates a typical latitude variation with altitude near perigee for OGO-6 during this period. This figure is for orbit 555 on 14 July 1969. The perigee was near 40°N and the local time was 1425 hours. The microphone gage density measurement threshold is about 4×10^{-15} g cm^{-3}. This density usually occurred between 430 to 440 km. For example, if the threshold density occurred at 430 km, then (from Figure 4-1) the density gage gave meaningful values over a latitude range from about 15° to 65°N, or over a latitude range of 50°.

Figure 4-2 shows density versus geomagnetic latitude for orbits 548 to 553 on 13 July 1969 (a magnetically-disturbed day, $A_p = 14$). The solid curves are drawn between microphone gage density points normalized to 406 km. The first three orbits (548-550) exhibit the usual tendency for the density to increase from high to mid latitude. The mid-latitude density maximums (peaks) change their position markedly or appear and disappear from orbit to orbit. This is what is normally observed over the indicated latitude range. However, orbits 551 and 552 have their highest densities occurring at the high latitudes. An unusual pair of density peaks are present on both orbits; the first peak is at latitude 53°N, the second at 61°N. For orbit 551, the first maximum represents a density increase over several degrees of latitude, with the peak increase being 35 percent. The second maximum has a peak density increase of 39 percent. The second peak is located at 61°N for three consecutive orbits (550-552). It is

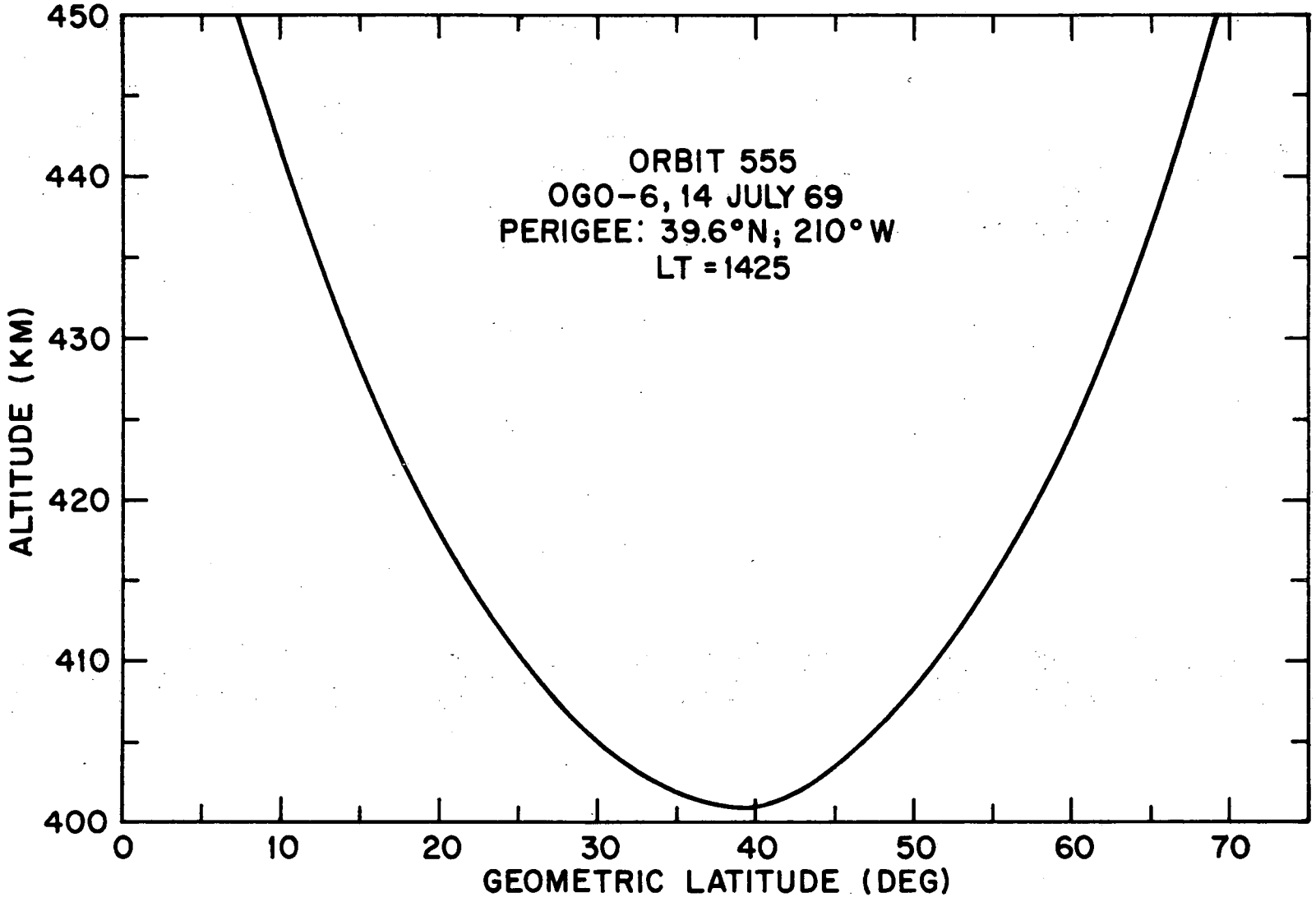

Fig. 4-1 OGO-6 latitude versus altitude variation near perigee on orbit 555, 14 July 1969.

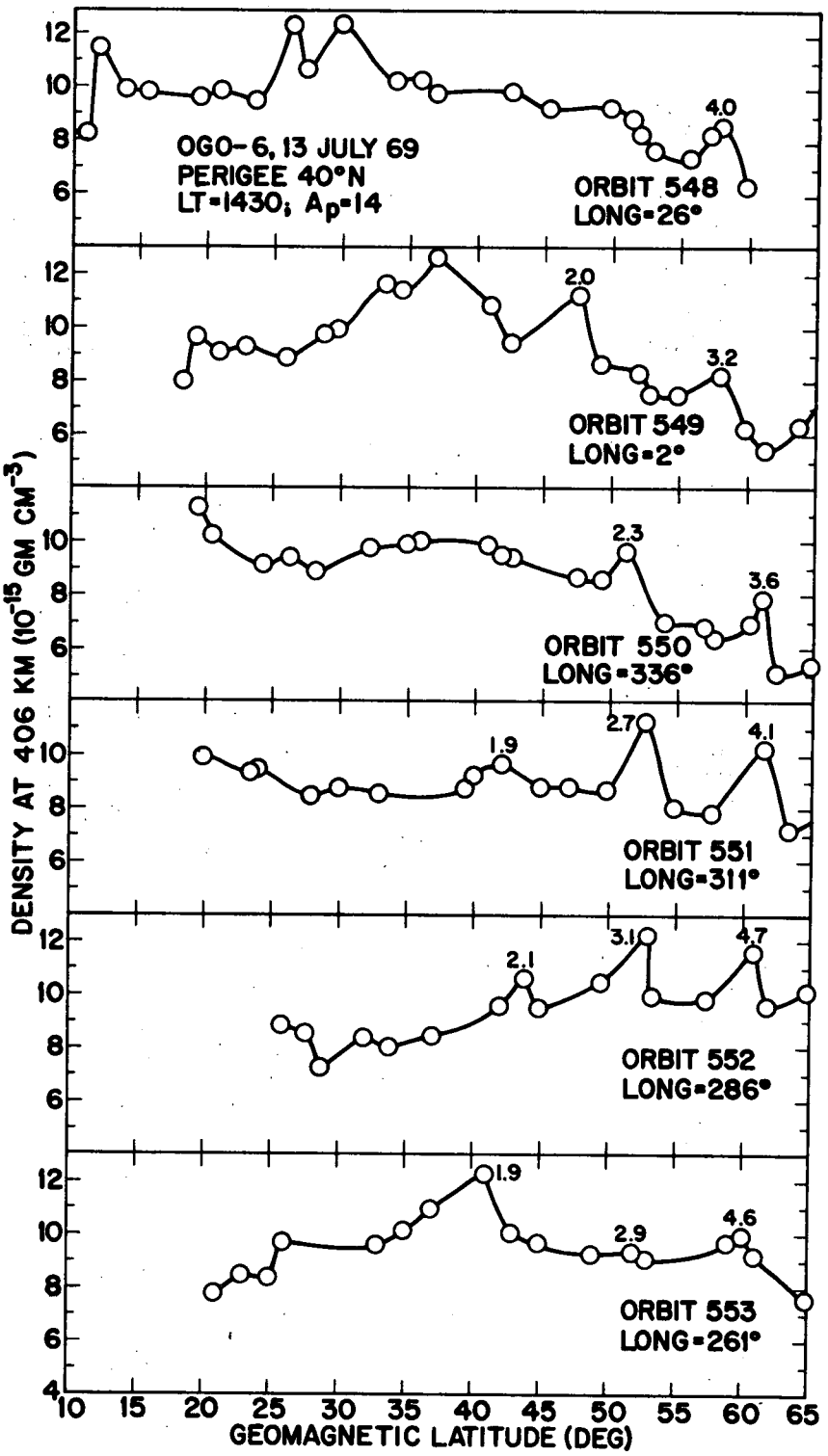

Fig. 4-2 OGO-6 density versus geomagnetic latitude for orbits 548 to 553, 13 July 1969 (a magnetically-disturbed day A_p = 14). The solid curves are drawn to density points derived from the Lockheed Microphone Gage normalized to 406 km altitude. L-values are listed at the top of the density peaks from 51°N to 61°N.

located at either 60°N or 61°N for six consecutive orbits (550-555). The high degree of reproducibility in location of this peak further indicates that the microphone density gage is measuring relative density variations accurately.

The first peak is located on L-shells with values between 2.3 and 3.1 and at latitudes 51°N to 53°N for orbits 550 to 553 (Figure 4-2). For the same orbits, the second peak is located on L-shells with values 3.6 to 4.7 and at latitudes 60°N or 61°N. Stable auroral red (SAR) arcs have been observed in L-shells 2.1 to 4.5 [Hoch and Smith, 1971] which lie approximately between geomagnetic latitudes 40 to 60°N. This suggests that the heating causing these density peaks may result from the same mechanism that causes SAR arcs at the same L-values, latitudes, and altitudes. Apparently, this is not the first time that a connection has been noted between neutral density and SAR arcs. Newton et al. [1965] mention that a density variation appearing in the Explorer 17 data on 1 June 1963 correlated with an increased zenith intensity of the 6300Å oxygen line.

The characteristics of the SAR arc are summarized by Roach and Roach [1963], Cole [1965], Roble [1969], Hoch and Clark [1970] and Roble and Dickinson [1970]. The red arc has been observed to be persistent, homogeneous, and stable with a lifetime of 10 hours or longer with the predominant emission being the OI(^{1}D - ^{3}p) atomic oxygen transition line at 6300Å. The arc generally occurs in mid-latitudes well south of the auroral zone during times of geomagnetic storms. It extends several degrees in the meridional direction forming magnetically conjugate arcs aligned over constant L-shells. The arc generally extends over a 300-700 km height interval with peak emission at an altitude of roughly 400 km. Satellite measurements of electron temperature in the near vicinity of a red arc show a considerable enhancement of the electron temperature in the arc region compared to the region outside the arc [Norton and Findlay, 1969].

Hoch and Clark [1970] report the probable occurrence of an SAR arc on 13-14 July 1969 (both geomagnetically-disturbed days). R. W. Owen [private communication, 1971] reports that for a brief period of time, around 0115 PST (0915 UT) on the night of 13-14 July 1969, there was an arc, particularly in the lower elevations. It was quite discernible from 15 to 30 degrees elevation. At other times and elevations, due to weather conditions or the general weakness of the arc, there was little or no evidence of arcs. This observation was made near Richland, Washington (geomagnetic latitude 53°N, longitude 299°E). The L coordinate associated with the observational site (2.7 at an altitude of 400 km) is the same as that associated with the density peak of 53°N, 314°E, on orbit 551 (Figure 4-2). Hence, the altitude, latitude, and L number are the same. The longitudes differ by only 15°. However, the density peak of orbit 551 occurs about 15 hours earlier than the SAR-arc observation of Owen. A strong peak occurred on orbit 566, about 24 hours later than orbit 551, when OGO-6 was at about the same longitude (295°E) as the SAR-arc observation, at 57°N latitude where L = 3.6 (Figure 4-3). No density peaks were noted on orbits 558 to 562, whose perigee longitudes ranged from 35°E to 135°E, several hours before and after the red arc was observed on 14 July 1969. The peak that occurred closest in time with Owen's arc observation was on orbit 563 at 1349 UT (or about four and one-half hours later) at 56°N, 10°E, where L = 3.0 (Figure 4-3).

Some of the above results are summarized in Table 4-1. This table lists the density peaks which appeared between 50°N and 61°N during 12-15 July 1969, a period that covers about one and one-half days before and after Owen's observation and includes some 50 orbits of data. Listed with each density peak is the geomagnetic latitude, L number, and associated density and temperature change. Also, K_p, the perigee universal time (UT) and longitude is listed for each orbit. A density peak is listed for an orbit in Table 1 only if the peak shows good continuity with regard to latitude or L number with peak (s) appearing in preceding or following orbits. The greatest difference in latitude between a peak with that of the next peak in the nearest orbit is four degrees. The average latitude difference is 1.3 degrees.

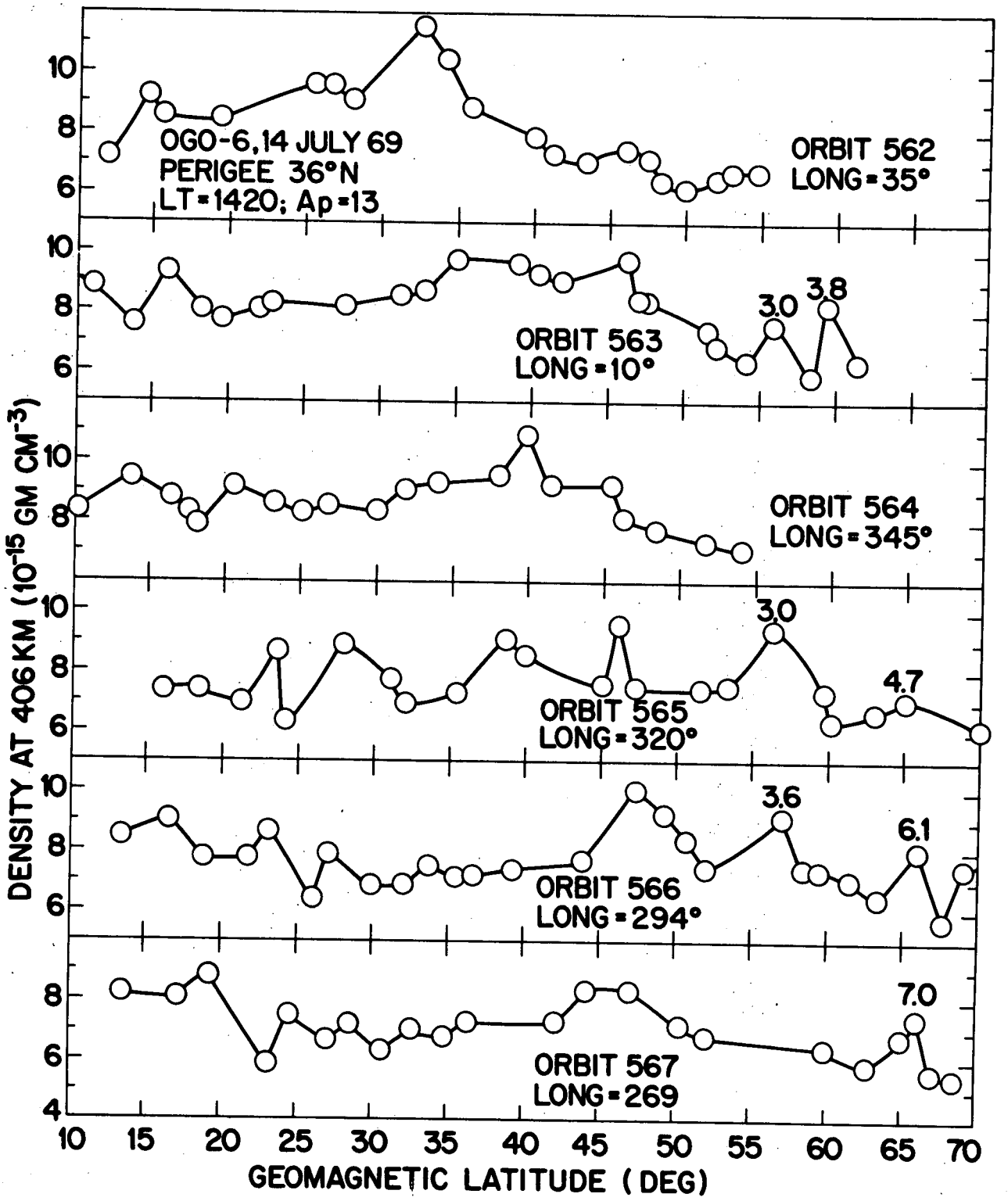

Fig. 4-3 OGO-6 density versus geomagnetic latitude for orbits 562 to 567, 14 July 1969 (a magnetically-disturbed day, A_p = 13). The solid curves are drawn to density points derived from the Lockheed Microphone Gage normalized to 406 km altitude. L-values are listed at the top of the density peaks from 55°N to 57°N.

Density peaks (maximums) appearing in OGO-6 microphone density gage data during 12-15 July 1969, listed according to orbit, K_p, perigee universal time and longitude. The first peak has L values from 2.3 to 3.6; the second has L values from 3.6 to 4.7. Also listed for each peak is the geomagnetic latitude and density change.

					First Peak			Second Peak		
Date	Perigee UT	Orbit	K_p	Longitude of Perigee (Deg) E	Geomagnetic Lat (Deg)	L	Density Change (Percent)	Geomagnetic Lat (Deg)	L	Density Change (Percent)
12 July	1339	534	1.67	17						
	1520	535	1.33	352	52	2.3	15	61	3.7	44
	1700	536	1.33	327	56	2.8	19			
	1839	537	2.67	302				61	4.3	31
	2019	538	2.67	277	54	3.2	11			
	2157	539	4.00	252	No data					
	2338	540	4.00	227	55	3.2	35			
13 July	0118	541	2.67	202						
	0258	542	2.67	177						
	0438	543	3.33	152	52	3.1	42	57	4.0	40
	0618	544	3.00	127	50	3.1	17			
	0757	545	3.00	102						
	0935	546	3.33	77	No data					
	1114	547	3.33	52				56	4.2	10
	1255	548	2.00	27				58	4.0	25
	1435	549	2.00	2						

(Cont'd)

TABLE 4-1 (Cont'd)

Date	Perigee UT	Orbit	K_p	Longitude of Perigee (Deg) E	First Peak			Second Peak		
					Geomagnetic Lat (Deg)	L	Density Change (Percent)	Geomagnetic Lat (Deg)	L	Density Change (Percent)
13 July	1615	550	2.00	337	51	2.3	20	61	3.6	44
	1755	551	2.00	312	53	2.7	35	61	4.1	39
	1933	552	3.67	287	53	3.1	22	61	4.7	21
	2113	553	2.33	261	52	2.9	3	60	4.6	22
	2252	554	2.33	235	55	3.1	8	60	4.1	30
14 July	0033	555	2.33	210	54	3.2	18	61	4.5	22
	0212	556	2.33	185	54	3.2	17	59	4.5	23
	0351	557	4.67	160	53	3.1	28			
	0531	558	4.67	135						
	0711	559	2.33	110						
	0850	560	2.33	85						
	1030	561	1.67	60						
	1209	562	3.33	35						
	1349	563	3.33	10	56	3.0	23	60	3.8	37
	1528	564	2.00	345						
	1709	565	2.00	320	56	3.0	34			
	1849	566	2.00	295	57	3.6	23			

(Cont'd)

TABLE 4-1 (Cont'd)

Date	Perigee UT	Orbit	K_p	Longitude of Perigee (Deg) E	First Peak			Second Peak		
					Geomagnetic Lat (Deg)	L	Density Change (Percent)	Geomagnetic Lat (Deg)	L	Density Change (Percent)
14 July	2029	567	2.00	270						
	2207	568	2.00	245						
	2346	569	2.00	220	55	3.2	49			
15 July	0126	570	1.33	195	No data					
	0306	571	1.33	169	No data					
	0446	572	1.33	144						
	0625	573	1.67	119						
	0805	574	1.67	94						
	0945	575	1.33	69						
	1125	576	1.33	44						
	1304	577	1.33	18						
	1444	578	1.33	353						
	1623	579	0.67	328						
	1803	580	1.00	303	54	3.0	31			
	1943	581	1.00	278	56	3.4	40			
	2123	582	2.00	253	No data					
	2302	583	2.00	228	58	3.6	27			

The greatest difference in L-value is 0.6, and the average difference is 0.3. The L-value connected with the lower latitude peak (first peak) varies between 2.3 and 3.6 (average L is 3.0). The associated geomagnetic latitude varies between 50°N and 58°N (average is 54°N). The L-value for the high latitude peak (second peak) varies from 3.6 to 4.7 (average L is 4.2). The associated latitude varies from 56°N to 61°N (average latitude is 60°N). The average invariant magnetic latitude for the low and high latitude peaks is 53 and 60°N, respectively. The average density change represented by the 34 peaks was 27 percent. The low-latitude peak appears on 21 orbits, the high-latitude one on 13 orbits. In cases where multiple peaks occurred on the same orbit, the low-latitude peak exhibited an average density change of 20 percent, the high-altitude one 32 percent. Both appear on seven successive orbits on 13-14 July (550 to 556), or almost halfway around the world. Multiple peaks appear on ten orbits. The high-latitude peak appeared alone only in three out of 13 orbits. Obviously, in most cases the peaks are temporally connected. Roble [1969] states that in certain cases multiple arcs form along different invariant magnetic latitudes and in these cases the lower latitude arcs are more stable. Roach and Roach [1963] present evidence of three and possibly four parallel arcs on 12-13 November 1960. In Table 4-1, two density peaks are listed for orbit 543, 13 July 1969. However, two others were present: one at latitude 44°N with L = 2.2; another at latitude 48°N with L = 2.6. Three peaks occur on orbit 552 (Figure 4-2). The peak at latitude 44°N has an L = 2.1. No density peaks appeared at longitudes from 51 to 127°E during 13-15 July. Hence, the data in Table 4-1 indicate that the peaks are not global in extent but favor the 150 to 350°E longitude sector. The data in Table 4-1 indicate that the low-latitude peak persisted around longitude 300°E, near the longitude of Owen's SAR-arc observation, for at least two days, from 13-15 July 1969.

Most of the peaks in Table 4-1 definitely appear with L-values and latitudes associated with SAR arcs. Some of the high-latitude peaks may be associated with aurora, especially those with L-values greater than 4.0 and latitudes greater than 60°N. Some density peaks with L numbers greater than 4.7 and latitudes greater than 61° were not listed in Table 4-1 since they did not follow the somewhat strict continuity conditions. Hoch and Clark [1970], reporting on SAR arcs observed between September 1967 and mid may 1969, state that on every occasion of an SAR arc there was also a polar auroral display to the north.

Geomagnetic control over the SAR arcs is indicated by the fact that they are usually observed during periods of increased magnetic activity and that their intensity normally increases with the magnetic activity index K_p [Roach and Roach, 1963]. K_p is listed for each orbit in Table 4-1. The average K_p associated with the 34 density peak is 2.46. The average for no peaks is 2.13 (56 cases). This does not indicate a strong correlation between K_p and the occurrence of the density peaks. Figure 4-4, a plot of K_p and peak occurrence versus universal time, confirms that there is not a strong correlation between them. The relationship between K_p and SAR-arc occurrence is not well established. Roble et al. [1970] give an example of a red arc on 31 October 1968 that disappeared even though K_p continued to increase. The SAR arc reported by Owen occurred near a K_p minimum at 0915 UT, 14 July 1969 (Figure 4-4).

4.1.1 Temperature Increase in Density Peaks

Using a model atmosphere, one can estimate the amount of heating (temperature change) connected with the density peaks. Figure 4-5 shows the density at 400 km associated with a given exospheric temperature at local time 1400 [Anderson and Francis, 1966] where the solid curve is drawn to the three points, $S' = 50$, $S' = 125$, and $S' = 200$, where S' represents the solar activity (heating) in radioastronomy units (10^{-22} w m^{-2} hz^{-1}) of 10.7-cm flux. The temperature change associated with a given density change can be estimated from Figure 4-5.

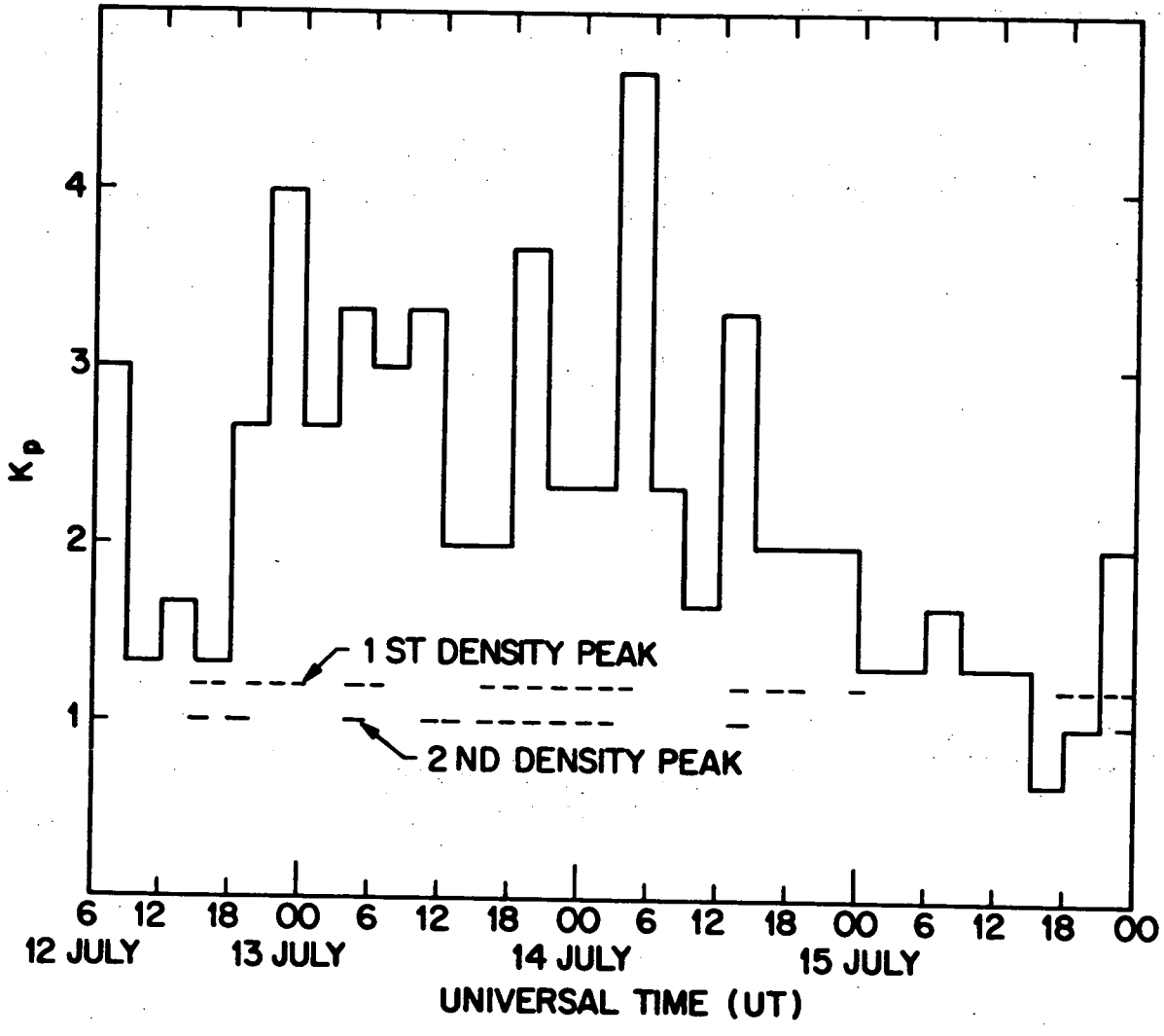

Fig. 4-4 K_p versus universal time (UT) from 06 UT 12 July 1969 to 00 UT 16 July 1969. The times of occurrence of the first and second density peaks listed in Table 4-1 are indicated by dashed lines. The SAR arc reported by Owen occurred on 14 July 1969 at 0915 UT near a K_p minimum.

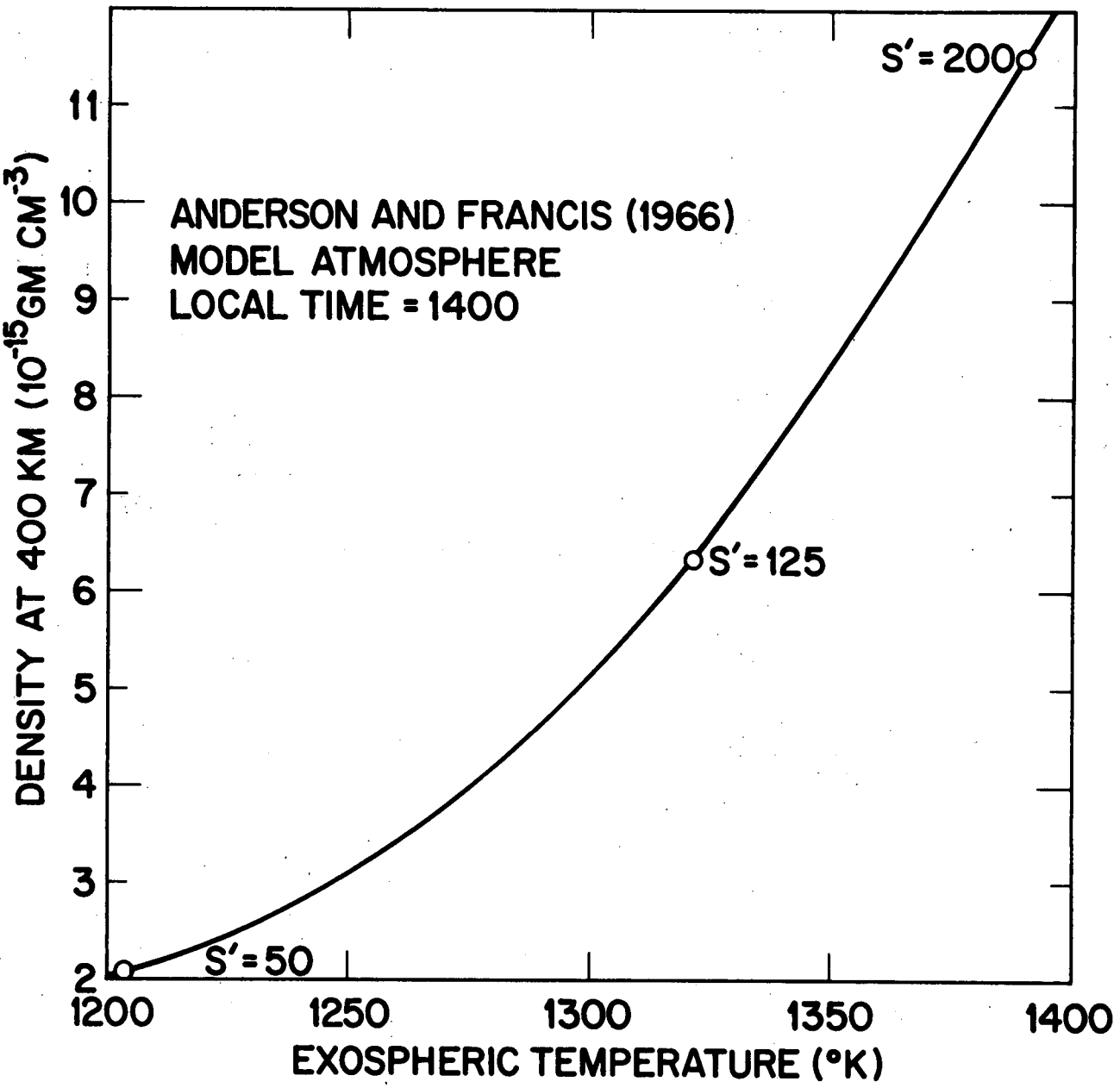

Fig. 4-5 Density at 400 km versus exospheric temperature at local time 1400 from Anderson and Francis (1966) model atmosphere. The solid curve is drawn to S' data points, where S' represents the solar activity in radioastronomy units (10^{-22} w m^{-2} Hz^{-1}) of 10.7-cm flux.

These temperature changes are listed in Table 4-1 for each peak. Inasmuch as the temperature change estimates depend mainly on relative density variations, they are fairly accurate. The temperature changes ranged from $4^{\circ}K$ (orbit 553, first peak) to $41^{\circ}K$ (orbit 551, second peak and orbit 569, first peak). The average temperature change associated with the 34 peaks was $25^{\circ}K$. The intensity of the SAR arc corresponding to $K_p = 2.45$ (the average value associated with the density peaks) is estimated to be 500 Rayleighs (R) [Roach and Roach, 1963], indicating a weak SAR arc. The SAR-arc observation of Owen, discussed previously, also indicated a weak arc. Roble [1969] theoretically predicts a temperature increase of $30^{\circ}K$ for a 600R arc, based on a thermal conduction model of the arc. Hence, our average temperature increase of $25^{\circ}K$ associated with a 500R arc is in good agreement with theory based on thermal conduction. Also, the small amplitude of the temperature increase within the SAR arc is consistent with Doppler measurements for the 31 October/1 November 1968 red arc with intensity from 100R to 600R [Roble, Hays and Nagy, 1970]. The data showed no measureable neutral gas temperature increase within the red arc compared to temperatures measured in regions outside the arc. The error limits of the instrument were estimated at $\pm 75^{\circ}K$.

4.1.2 SAR Arc Mechanisms

Various mechanisms have been suggested for the SAR arc. These mechanisms are the recombination hypothesis [King and Roach, 1961], the electric field hypothesis [Rees, 1961; Megill and Van Zandt, 1964; Walker and Rees, 1968], the soft electron flux hypothesis [Dalgarno, 1964], and the thermal conduction hypothesis [Cole, 1965]. The last three mechanisms have been considered by Chandra et al. [1970] who conclude on the basis of observational data on electron temperature and the flux of superthermal electrons that the thermal conduction hypothesis proposed by Cole is clearly the mechanism for heating the ambient plasma during the SAR-arc condition. All four excitation mechanisms have been reviewed by Roble [1969] who concludes that the thermal

hypothesis of Cole is consistent with the observational data and offers a mechanism for the transfer of energy from the magnetosphere to the ionosphere. Further support for the thermal conduction hypothesis is offered in this paper by the agreement of the estimates of the magnitude of the neutral temperature changes associated with the density peaks with those predicted by Roble [1969] for SAR arcs from a thermal conduction model.

Cole [1965] assumes that the SAR arc is excited by the impact of local thermal electrons in the F-region with atomic oxygen and that the F-region electrons are kept sufficiently hot by thermal conduction from the magnetosphere in the electron-ion gas along geomagnetic field lines. Conduction in the electron-ion gas proceeds downward to a "transition" level (380-550 km altitude) where transfer of heat to neutrals absorbs the heat flux. Below this height, conduction in the neutrals dominates. Cole urges that an atmospheric bulge should exist in the vicinity of the SAR arc because of electron heating of the neutral gas within the arc. Because the thermosphere is in diffusive equilibrium, the neutral temperature increase with the SAR arc will cause a thermal expansion of the atmosphere, resulting in a density bulge. Roble [1969] demonstrates that thermal equilibrium is rapidly approached in the SAR arc because the arc is persistent and stable and the conduction time constant is short compared to the lifetime of the arc.

The SAR-arc formation mechanism of Cole [1965] predicts that the arc will be found at the point of decreasing ambient ion density in the magnetosphere, the plasmapause. This is supported by Chappell, Harris and Sharp [1971] who show that the SAR arcs are observed in the rapid recovery phase of the storm in the 10-20 hours following injection of ring current particles, and that the plasmasphere is drastically reduced in size during the storm, with the SAR arc located in L-value near the position of the plasmapause.

4.2 Variation of Atmospheric Density with Geomagnetic Activity

The material in this section is based on the density data measured by this instrument at low latitudes on 110 orbits for the period 25 September through 3 October 1969. During this period the satellite perigee was between 10° and 25°N latitude at 1540 to 1630 local time. The 10.7 cm solar flux varied between 132.5 and 169.3 R.U. (Radio-astronomy Units). This period was selected because several geomagnetic storms occurred. Hence, there was a large variation in the magnetic indices K_p and a_p (a_p varied from 0 to 207). This provided an opportunity to study the relationship between neutral density changes and magnetic variations at low latitudes, as a function of latitude, longitude, and time.

The U. S. Space Science Board of the National Academy of Sciences (1968) concludes that the response of the global circulation to high latitude heating is one of the most provocative questions facing us at present. Although it is known that the density of the whole neutral upper atmosphere varies with geomagnetic activity, the relationship between the density changes and the geomagnetic activity, as represented by a_p or K_p, has not been well established. Empirical equations based on satellite-drag data are not very accurate. Transient density fluctuations associated with geomagnetic activity are difficult to study by the satellite-drag analysis method because the time and spatial resolutions are so large. This task is also difficult because the quantity to be determined, the acceleration of the satellite's mean motion, is the second derivative of the mean anomaly. Another limitation exists because the change in the orbital period is a measure of the integrated effect of air drag in the neighborhood of perigee. Localized values of density cannot be provided, but only values averaged over an arc of 30° or more.

The quadrupole mass analyzer on OGO-6 was used to study neutral composition variations during the period between 27 September and 1 October 1969. These measurements by Taeusch et al (1971) provided observations of composition variability that showed a significantly different behavior of the atmosphere during a magnetic

storm than the behavior deduced from the lower-resolution total mass density determined from satellite-drag measurements. The composition data indicated that the major effect of a magnetic storm on the neutral atmospheric components above 400 km altitude is localized in the high-latitude regions of the earth at magnetic latitudes above 50°, and the response time of the atmosphere to such storms is less than one hour. However, the analysis of the data from the Lockheed microphone density gage indicates that the density changes significantly with magnetic activity even at low latitudes. For example, the average density at 406 km and 1600 hr LT between 0° and 30°N latitude was 38 percent higher on 29 September 1969, a magnetically disturbed day (A_p = 71) than on 27 September 1969, a quiet day (A_p = 6). The 10.7 cm solar flux was 151.3 R.U. on September 27 and 139.9 R.U. on September 29, where R. U. is a Radioastronomy Unit (10^{-22} w m^{-2} Hz^{-1}).

4.2.1 Atmospheric Density Variation with K_p (or a_p)

Figure 4-6 shows some typical latitudinal density profiles for 27-30 September 1969 at 406 km and 1600 Hr local time from about 0° to 40°N for K_p equal to 0, 4+, 6 and 8, respectively. These density profiles are fitted to density points derived from the microphone density measurements [Anderson and Sharp, 1972], made over an altitude range near perigee averaging about 20 km. An atmospheric model [Anderson and Francis, 1966] was used to normalize the data to an altitude of 406 km. The resulting data points in Figure 4-6 have an average time separation of one-half minute and an average distance separation of 2 to 3 degrees. The 10.7 cm solar flux varied slightly during 27-30 September 1969, from 151.3 R. U. to 137.0 R.U. The curves of Figure 4-6 indicate that the 406 km density definitely increased at all latitudes with increasing geomagnetic activity, represented by K_p. The average density from 10°N to 20°N is over twice as great for K_p = 8 as K_p = 0. The curve for K_p = 8 (orbit 1684) indicates a broad maximum with three peaks from 15°N to 35°N. Many curves from

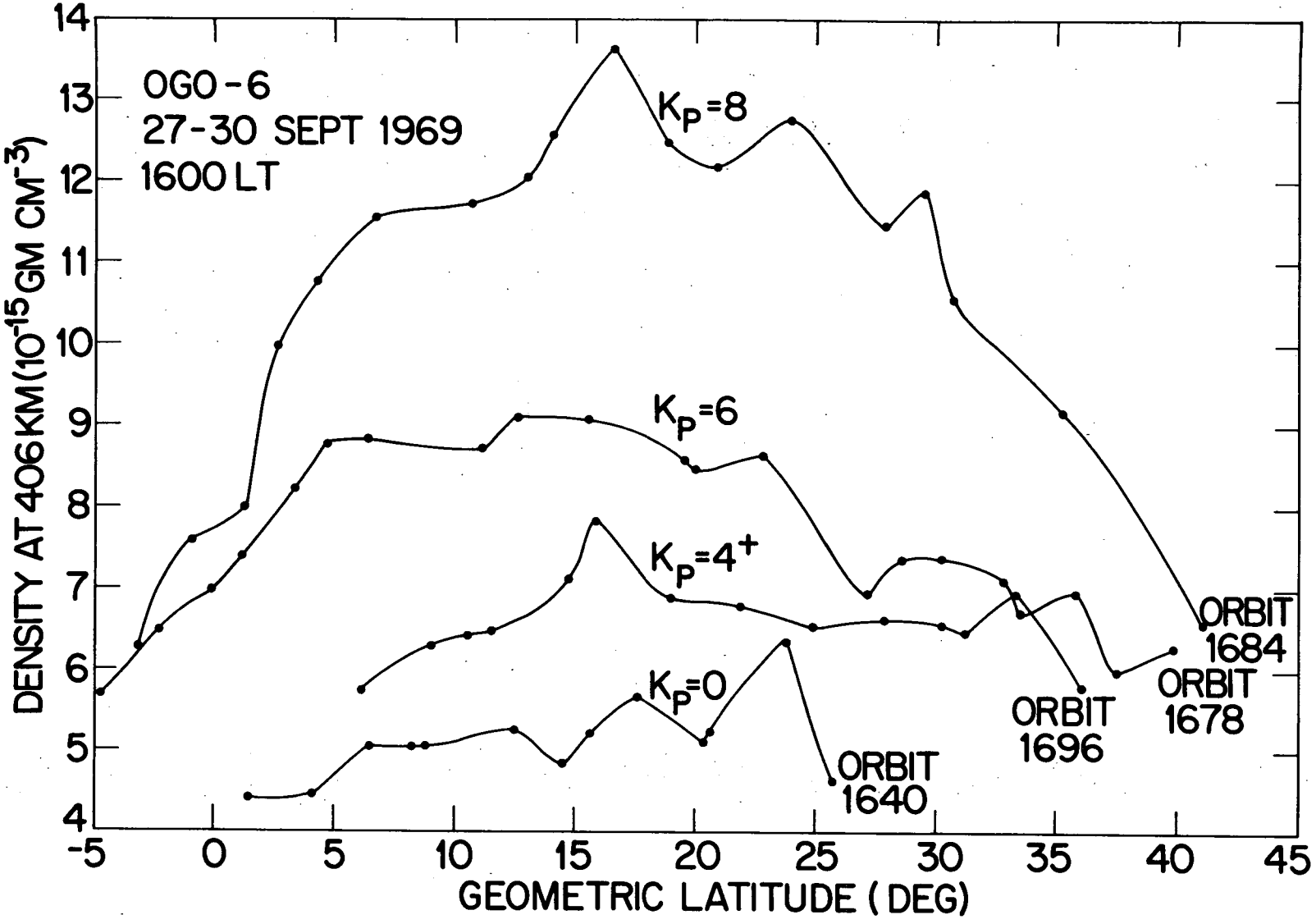

Fig. 4-6 Some typical latitudinal density profiles for 27-30 September 1969 at 406 km and 1600 LT from 0° to 40°N latitude for K_p = 0, 4+, 6, and 8. These density profiles are fitted to density points derived from the Lockheed Microphone Density Gage measurements (Anderson and Sharp, 1972).

other orbits during 25 September - 3 October 1969 present a similar broad maximum, with much lower densities near the equator and above 40°N, especially those curves associated with high K_p, indicating geomagnetic disturbed conditions. This low-latitude density bulge which seems to be a permanent feature near the equinoxes, was first found by analyzing drag data from Explorer 1 in 1961 and 1962 [Anderson, 1966]. Newton and Pelz (1969) analyzing in-situ density measurements from Explorer 32 density gages for May through October 1966 during geomagnetically quiet days, concluded that the low mid-latitude density can be 20 percent greater than the equatorial density during the day for altitudes between 300 and 400 km. Hedin and May (1971) fround maxima in the N_2 and O densities measured by the mass spectrometer on OGO-6 at $\pm$ 20° magnetic latitude during July and September 1969.

The low-latitude density bulge illustrated in Figure 4-6 may prove important for understanding the semi-annual effect appearing in satellite drag data. This effect is poorly understood at present. It is well known that there is a greater frequency of geomagnetic disturbances around the equinoxes. On the average, "magnetic" heating is indicated to be stronger near the Fall equinox than near the Spring equinox, with a minimum of heating from June to August and December to January. These features are also characteristic of the semi-annual effect. Based on this similarity, a recent explanation advanced for the semi-annual effect proposes that it is a complex effect resulting from both latitudinal density variations caused by solar heating and "magnetic" heating, with the former dominating during summer and winter and the latter dominating during Spring and Fall [Anderson, 1969].

Figure 4-7 shows two curves for the period 27-30 September 1969, where the solid curve is the density at 406 cm and 20°N geomagnetic latitude and the dashed curve is for K_p. From inspection, it is obvious that the higher densities are usually associated with high K_p.

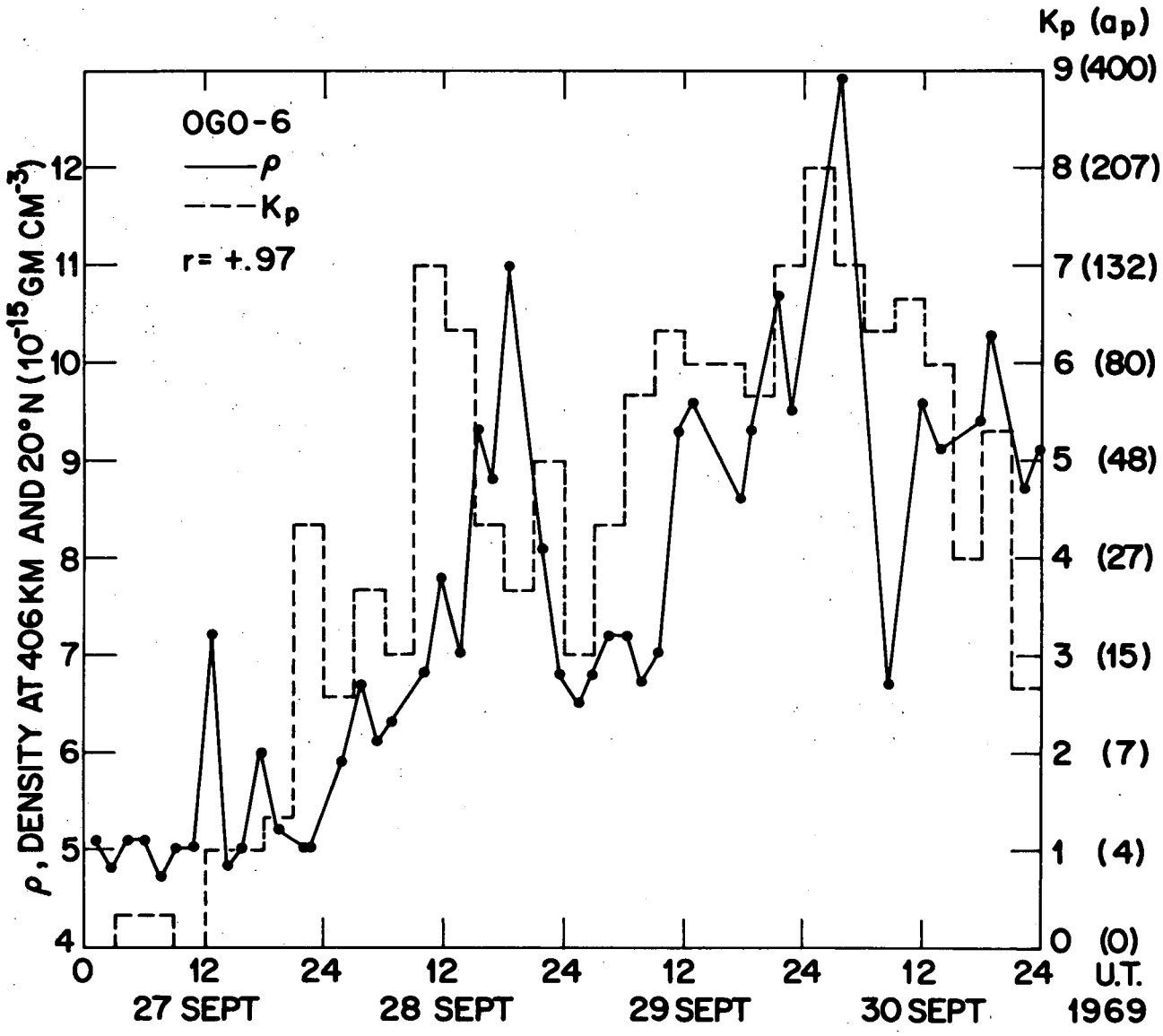

Fig. 4-7 Density and K_p versus Universal Time (UT) for 27 September through 30 September 1969. The solid curve is the density at 406 km and 20°N geomagnetic latitude, and the dashed curve is for K_p. The correlation coefficient between density and K_p is r = +.97. The values of K_p (and the corresponding a_p) are shown on the right.

The coefficient of correlation between density and K_p is r = +.97. K_p is interchangeable with a_p, as indicated on the right hand side of Figure 4-7.

4.2.2 Predictive Method

Inasmuch as Figure 4-7 indicated a good correlation between density and K_p (or a_p), a method was devised to derive predictive equations. The method consists in making least-squares straight-line fits to points on density-a_p scatter diagrams, where the density ρ at 400 km is delayed in 3-hr time intervals behind a_p from 0 to 24 hr. Equations of the fitted straight lines were derived for all the delay times for a given latitude or longitude sector. The corresponding standard error was calculated for each equation. The delay time which resulted in the best fit at a given latitude or longitude sector was found by selecting the equation having the minimum standard error. Hence, the best-fit equation was taken as that which resulted in a minimum standard error.

The equation of the least-squares straight line fit for the ρ, a_p points is

$$\rho_c = (a + b\, a_p)\ 10^{-15}\ \text{gm cm}^{-3}. \qquad (4\text{-}1)$$

The constants a and b are determined from the following normal equations:

$$\sum \rho = n\, a + b \sum a_p \qquad (4\text{-}2)$$

$$\sum (\rho\, a_p) = a \sum a_p + b \sum a_p^2, \qquad (4\text{-}3)$$

where n is the number of data points.

Solving (4-2) and 4-3),

$$a = \frac{\sum(\rho\, a_p)}{\sum a_p} + \frac{\sum a_p \sum \rho \sum a_p^2 - n\sum(\rho\, a_p)\sum a_p^2}{n\sum a_p \sum a_p^2 - (\sum a_p)^3}\,; \tag{4-4}$$

and,

$$b = \frac{n\sum(\rho\, a_p) - \sum a_p \sum \rho}{n\sum a_p^2 - (\sum a_p)^2}\,. \tag{4-5}$$

The standard deviation of the n data points about the line (4-1), or the standard error is,

$$S_\rho = \left[\frac{(\rho - \rho_c)^2}{n}\right]^{1/2}. \tag{4-6}$$

Equations (4-1), (4-4), (4-5), and (4-6) were programmed for computer calculation. For example, Figure 4-8 is a scatter diagram containing 80 data points at 10°N geomagnetic latitude from 26 September through 3 October 1969. The ordinate is ρ at 400 km in units of 10^{-15} gm cm^{-3}, and the abscissa is a'_p or the value of a_p at t - 3 hr, t being the time of the density values. The a'_p values range from 0 to 207 (K_p = 8), while ρ ranges from about 4.0 to 14.5 x 10^{-15} gm cm^{-3}. The equation of the least-squares solid line in Figure 4-8 is

$$\rho_c = (5.46 + .0336\, a'_p)\ 10^{-15} \text{ gm cm}^{-3} \tag{4-7}$$

The dashed straight lines in Figure 4-8 indicate the limits of the standard error, which is

$$S_\rho = 1.07 \times 10^{-15} \text{ gm cm}^{-3}, \tag{4-8}$$

or 16.0 percent of the average density. Some of the points contained

C-2

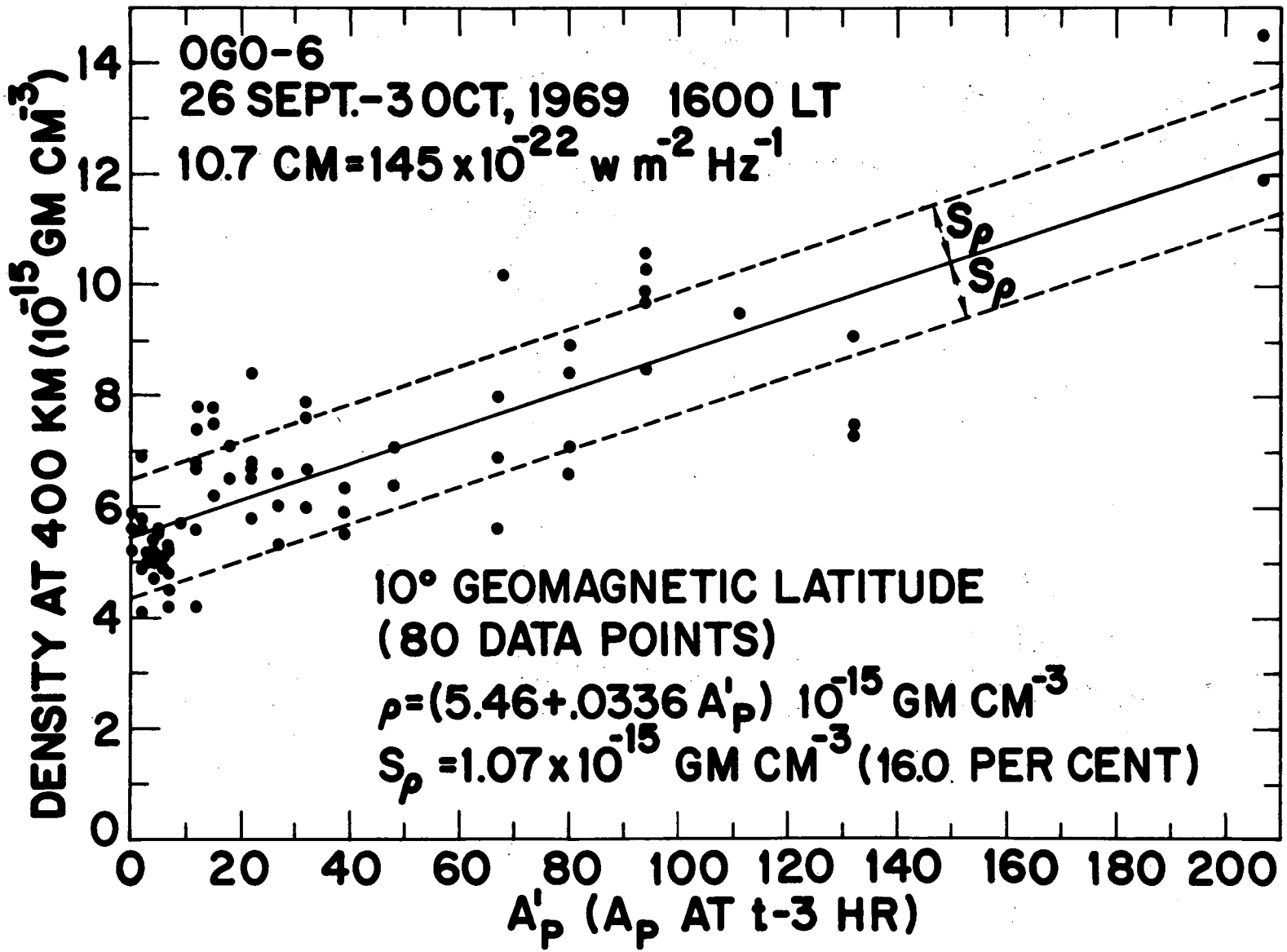

Fig. 4-8 Density at 400 km versus a'_p scatter diagram for 80 data points for 26 September - 3 October 1969 at 10°N geomagnetic latitude, 1600 LT, and 145 RU, where a'_p is the value of a_p at t-3 hr, t being the time of the density values.

outside the dashed straight lines are associated with peaks and troughs appearing in the latitudinal density profile (Figure 4-6).

The index a_p comes entirely from converting K_p to a normalized linear scale. The 3-hr planetary index K_p is obtained by averaging values from 12 observatories located between 47.7 and 62.5 geomagnetic latitude, averaging 56 degrees geomagnetic latitude. Thus a_p (or K_p) represents magnetic disturbances near 56 degrees geomagnetic latitude. The fact that a_p and K_p represent a mixture of disturbance effects associated with auroral electrojets, storm-time variations, and other magnetic variations of smaller amplitude such as sudden impulses makes them useful for very general correlations. However, for more discriminating studies it is desirable to have indices for each type of disturbance. Since we are interested in low-latitude effects, it was decided to investigate the Equatorial D_{st} magnetic activity index [Hess, 1965; Siguira and Cain, 1969). Equatorial D_{st} is a measure of the mean departure from normal of the horizontal component, H, of the Earth's magnetic field observed at a group of low-latitude stations, whereas a_p is based on 3-hr ranges of the field at stations in higher latitudes.

Accordingly, the D_{st} magnetic index was selected to find if more accurate least-squares fits could be achieved on density versus D_{st} scatter diagrams. Not only does the type of magnetic storm variation represented by D_{st} occur at low and moderate latitudes, but the D_{st} values themselves are avilable every hour, instead of every 3 hours like a_p. This could be an advantage when studying the relationship of magnetic storms with rapid changes in the density. However, D_{st} can be positive or negative. The negative values, especially the larger ones, are normally associated with ring-current particle injection associated with magnetic storms.

The equation for the least-squares straight line fit for the ρ, D_{st} points is

$$\rho_c = (a' + b'D_{st})\ 10^{-15}\ \text{gm cm}^{-3} \qquad (4\text{-}9)$$

where the constants a' and b' are determined from normal equations

similar to (4-4) and (4-5) with D_{st} substituted for a_p.

As an example, Figure 4-9 is a scatter diagram of density at 400 km versus D_{st} at t hr. corresponding to 89 density data points at 20°N (Figure 4-8). The D_{st} values range from -113 to 45. The equation of the least-squares straight line is

$$\rho_c = (6.51 - .0256D_{st})\ 10^{-15}\ \text{gm cm}^{-3} \qquad (4\text{-}10)$$

The standard error is

$$S_\rho = 1.69 \times 10^{-15}\ \text{gm cm}^{-3} \qquad (4\text{-}11)$$

or 23.6 percent of the average density.

4.2.3 Analytic Comparison

Table 4-2 represents the constants a and b in Equation (4-1) computed from (4-4) and (4-5) for a_p from time t to t - 24 hr in 3-hr increments and geo-magnetic latitudes 0°N, 10°N, 20°N, 30°N, and 40°N and all latitudes (0°N to 40°N). Table 4-3 exhibits the corresponding standard error S_ρ, expressed in percent of the average density of the n data points, calculated from (4-6) and (4-1). In addition, S_ρ is given for $a_p < 15$ and $a_p > 15$, representing quiet and disturbed geomagnetic conditions, respectively. The minimum standard error in each column is marked with an asterisk. This value can be used to determine the time delay between ρ and a_p that gives the best correlation in a given column. For example, under the 10°N column the minimum S_ρ occurs for a_p at t - 3 hr. The corresponding a and b selected from Table 4-2 results in Equation (4-7) (see Figure 4-8). Displayed at the bottom of each column in Table 4-3 is the average S_ρ, the ratio of the average S_ρ to the minimum S_ρ, the number of data points n, and the relative density (density for "all latitudes" = 1.00). The minimum S_ρ occurs at 0°N, 10°N, and 20°N for a_p at t - 3 hr and at 30°N and 40°N for a_p at t-9 hr. However, no significance is attached to the minimum values at 30°N and 40°N because the average/minimum S_ρ ratios are low. It doesn't matter greatly which time delay

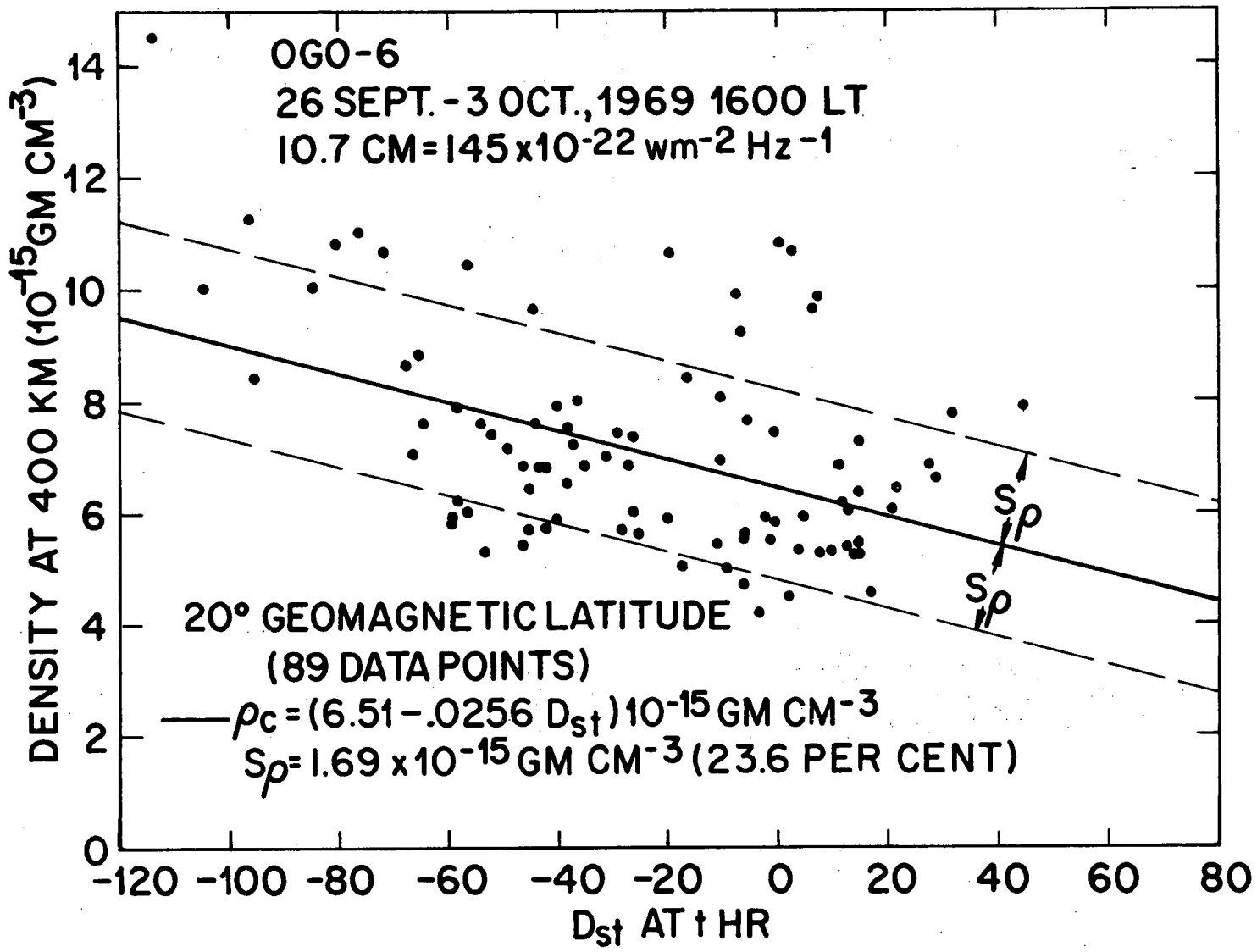

Fig. 4-9 Density at 400 km versus D_{st} scatter diagram for 89 data points for 26 September - 3 October 1969 at 20°N geomagnetic latitude, 1600 LT, and 145 RU, where D_{st} is at time t, t being the time of the density values. The solid straight line represents the least-squares fit to the data points. The standard error limits are indicated by the dashed straight lines.

TABLE 4-2

a AND b FOR LATITUDE AND TIME

TIME OF a_p (hr)	GEOMAGNETIC LATITUDE										ALL LATITUDES	
	0° N		10° N		20° N		30° N		40° N			
	a	b	a	b	a	b	a	b	a	b	a	b
t	5.12	.0297	5.72	.0261	6.06	.0289	6.18	.0278	6.87	.0151	5.95	.0271
t-3	5.24	.0262	5.46	.0336	5.80	.0371	6.26	.0241	6.65	.0184	5.78	.0303
t-6	5.45	.0226	5.68	.0289	5.84	.0369	6.16	.0271	6.72	.0145	5.87	.0287
t-9	5.66	.0207	6.02	.0215	6.00	.0339	6.17	.0294	6.59	.0184	6.03	.0271
t-12	5.58	.0231	6.04	.0196	6.05	.0300	6.31	.0232	7.08	.0081	6.11	.0231
t-15	5.45	.0360	6.12	.0179	6.29	.0245	6.52	.0187	7.03	.0090	6.23	.0207
t-18	5.44	.0287	5.88	.0265	6.34	.0231	6.52	.0194	6.89	.0137	6.16	.0230
t-21	5.60	.0193	5.93	.0262	6.63	.0149	6.83	.0110	7.19	.0087	6.38	.0167
t-24	5.72	.0173	6.10	.0195	6.63	.0152	6.93	.0086	7.16	.0107	6.44	.0154

TABLE 4-3

a_p, STANDARD ERROR FOR LATITUDE AND TIME

TIME OF a_p (hr)	GEOMAGNETIC LATITUDE					ALL LATITUDES	ALL LATITUDES ($a_p < 15$)	ALL LATITUDES ($a_p > 15$)
	0° N	10° N	20° N	30° N	40° N			
t	15.7	21.5	21.2	18.9	13.9	20.3	21.2	18.9
t-3	14.1*	16.0*	15.5*	19.4	13.9	17.5*	16.8	16.8*
t-6	19.3	20.3	16.7	18.4	14.4	19.1	16.5*	19.3
t-9	22.2	24.5	19.8	18.0*	13.2	21.0	19.0	20.4
t-12	21.6	24.6	20.6	20.0	15.3	21.8	21.0	20.8
t-15	20.0	24.8	22.4	21.2	14.8	22.4	21.8	20.8
t-18	20.6	23.7	23.4	21.5	13.5	22.4	21.2	21.6
t-21	22.4	23.7	25.2	23.1	15.5	24.0	22.0	22.6
t-24	23.4	24.8	25.2	23.6	15.7	24.3	22.8	22.7
AVE.	19.9	22.6	21.1	20.4	14.4	21.4	20.2	20.4
AVE/MIN	1.41	1.41	1.36	1.13	1.09	1.22	1.23	1.22
n	49	80	89	80	30	328	171	157
REL. DENSITY	.89	.96	1.03	1.04	1.08	1.00	.89	1.12

*Minimum.

is selected for a_p for these latitudes. As indicated at the bottom of Table 4-3, the relative density is slighly below normal for the lower latitudes and for "all latitudes" with $a_p < 15$, while it is slightly above normal for the higher latitudes and for "all latitudes" with $a_p > 15$.

Table 4-4 gives the constants a and b for 60-degree longitude sectors and for all longitudes (same as the "all latitude" column in Table 4-2). Table 4-5 presents the corresponding S_ρ. The average/minimum S_ρ ratio for $180^\circ E$ - $240^\circ E$ is 1.81. The minimum S_ρ occurs for a_p at t-3 hr. Hence, it is very advantageous to use a_p at t-3 hr and a and b in Table 4-4 at t-3 hr in Equation (4-1) for this sector. On the other hand, it doesn't matter very much which time delay is used for a_p in the $60^\circ E$ - $120^\circ E$ sector since the average/minimum S_ρ is only 1.11. As indicated at the bottom of Table 4-5, the relative density variation with longitude is slight between $0^\circ N$ and $40^\circ N$ geomagnetic latitude.

Table 4-6 gives the constants a' and b' (Equation 4-9) computed for D_{st} for times t to t-13 hr in 1-hr increments and geomagnetic latitudes $0^\circ N$, $10^\circ N$, $20^\circ N$, $30^\circ N$, $40^\circ N$ and "all latitudes" ($0^\circ N$-$40^\circ N$). Table 4-7 presents the corresponding standard error S_ρ. The minimum standard error (marked with an asterisk) occurs for D_{st} at time t, the same times as the density values, for each latitude except $10^\circ N$, where it occurs with a time delay of 2 hours. Yet, the average/minimum S_ρ ratios at the bottom of Table 4-7 are low, so not much confidence can be placed in any particular time delay.

Table 4-8 shows the constants a' and b' for 60-degree longitude sectors and "all longitudes". The constant b' is positive in the $60^\circ E$ to $120^\circ E$ sector from t hr to t-5 hr and in the $180^\circ E$ to $240^\circ E$ sector from t-8 hr to t-10 hr. This indicates that there is no correlation between density and D_{st} during these delay times at these longitudes.

TABLE 4-4

a AND b FOR LONGITUDE AND TIME

TIME OF a_p (hr)	LONGITUDE												ALL LONGITUDES	
	0° - 60°E		60°-120°E		120°-180°E		180°-240°E		240°-300°E		300°-360°E			
	a	b	a	b	a	b	a	b	a	b	a	b	a	b
t	5.53	.0375	5.99	.0140	5.59	.0340	5.72	.0296	6.17	.0202	5.95	.0459	5.92	.0271
t-3	5.30	.0342	6.24	.0137	5.93	.0220	5.41	.0357	5.60	.0484	5.76	.0400	5.78	.0303
t-6	5.60	.0310	6.57	.0035	5.73	.0356	5.27	.0577	5.69	.0409	5.60	.0339	5.87	.0287
t-9	6.23	.0199	6.59	.0041	5.50	.0503	5.08	.0753	5.54	.0310	5.95	.0329	6.03	.0271
t-12	6.30	.0175	5.93	.0288	5.54	.0448	5.42	.0379	5.74	.0209	6.45	.0291	6.11	.0231
t-15	6.21	.0218	6.41	.0117	5.67	.0295	5.84	.0237	5.85	.0332	6.88	.0139	6.23	.0207
t-18	6.04	.0317	6.49	.0071	5.65	.0197	5.39	.0542	6.28	.0202	6.68	.0197	6.16	.0230
t-21	5.96	.0384	6.08	.0138	5.96	.0147	6.08	.0331	6.58	.0090	6.56	.0297	6.38	.0167
t-24	5.81	.0319	6.03	.0131	6.36	.0091	6.82	.0048	6.13	.0240	6.55	.0366	6.44	.0154

Table 4 - 5

a_p, STANDARD ERROR FOR LONGITUDE AND TIME

TIME OF a_p (hr)	LONGITUDE						ALL LONGITUDES
	0° -60° E	60° -120° E	120° -180° E	180° -240° E	240° -300° E	300° -360° E	
t	19.6	14.5	13.0*	21.7	20.4	20.7	20.3
t-3	15.8*	15.7	14.0	13.5*	17.6*	19.3	17.5*
t-6	17.2	17.0	13.1	14.5	18.8	16.2*	19.1
t-9	22.0	17.2	14.5	20.3	17.6*	18.8	21.0
t-12	22.3	14.6	15.4	26.6	18.5	22.7	21.8
t-15	20.9	16.7	17.0	28.9	19.2	24.5	22.4
t-18	21.9	17.0	17.0	22.4	21.4	22.9	22.4
t-21	22.3	14.9	19.1	29.6	22.7	23.2	24.0
t-24	20.9	14.2*	21.2	33.2	20.0	24.0	24.3
AVE.	20.3	15.8	16.0	24.5	19.6	21.4	21.4
AVE./MIN	1.28	1.11	1.23	1.81	1.11	1.32	1.22
n	65	50	55	49	45	64	328
REL. DENSITY	1.02	0.97	0.96	1.00	1.00	1.06	1.00

*Minimum.

Table 4-6

a' AND b' FOR LATITUDE AND TIME

TIME OF D_{st}(hr)	GEOMAGNETIC LATITUDE										ALL LATITUDES	
	0° N		10° N		20° N		30°N		40° N			
	a'	b'	a'	b'	a'	b'	a'	b'	a'	b'	a'	b'
t	5.96	-.0245	6.28	-.0238	6.51	-.0256	6.65	-.0177	6.82	-.0170	6.37	-.0239
t-1	5.99	-.0218	6.29	-.0244	6.55	-.0249	6.78	-.0145	6.98	-.0139	6.42	-.0227
t-2	5.97	-.0202	6.30	-.0239	6.64	-.0213	6.95	-.0095	7.20	-.0096	6.50	-.0198
t-3	5.99	-.0177	6.36	-.0204	6.74	-.0175	7.07	-.0062	7.22	-.0101	6.58	-.0166
t-4	5.99	-.0163	6.37	-.0192	6.79	-.0153	7.15	-.0037	7.29	-.0079	6.62	-.0148
t-5	5.99	-.0140	6.40	-.0167	6.87	-.0120	7.27	.0001	7.48	-.0011	6.69	-.0114
t-6	6.00	-.0136	6.43	-.0150	6.90	-.0107	7.30	.0011	7.50	-.0004	6.73	-.0102
t-7	6.02	-.0107	6.46	-.0126	6.92	-.0095	7.27	.0003	7.42	-.0033	6.74	-.0093
t-8	6.01	-.0105	6.45	-.0131	6.95	-.0085	7.31	.0014	7.37	-.0053	6.75	-.0088
t-9	6.03	-.0094	6.47	-.0121	6.97	-.0081	7.30	.0013	7.41	-.0038	6.77	-.0080
t-10	6.04	-.0086	6.48	-.0114	6.97	-.0080	7.27	.0001	7.43	-.0030	6.77	-.0078
t-11	6.01	-.0105	6.47	-.0126	6.96	-.0083	7.25	-.0005	7.40	-.0037	6.76	-.0086
t-12	6.02	-.0114	6.46	-.0131	6.95	-.0090	7.20	-.0020	7.40	-.0034	6.74	-.0094

TABLE 4-7

D_{St}, STANDARD ERROR FOR LATITUDE AND TIME

TIME OF D_{St} (hr)	GEOMAGNETIC LATITUDE					ALL LATITUDES
	0° N	10° N	20° N	30° N	40° N	
t	21.2*	24.3	23.6*	22.6*	14.8*	22.7*
t-1	21.9	24.2	23.8	23.0	15.5	23.2
t-2	22.1	24.0*	24.6	23.5	15.7	23.6
t-3	23.0	25.1	25.2	23.8	15.6	24.3
t-4	23.7	25.5	25.7	24.0	15.9	24.7
t-5	24.3	26.0	26.1	24.0	16.3	25.3
t-6	24.5	26.3	26.2	24.0	16.3	25.4
t-7	25.0	26.6	26.4	24.0	16.1	25.4
t-8	25.0	26.4	26.5	24.0	16.1	25.6
t-9	25.1	26.6	26.5	24.0	16.1	25.6
t-10	25.1	26.6	26.5	24.0	16.1	25.6
t-11	25.0	26.4	26.5	24.0	16.1	25.4
t-12	25.0	26.4	26.4	24.0	16.1	25.4
AVE.	23.9	25.7	25.7	23.8	15.9	24.8
AVE./MIN	1.13	1.07	1.09	1.05	1.07	1.09
n	49	80	89	80	30	328
REL. DENSITY	.89	.96	1.03	1.04	1.08	1.00

*Minimum.

TABLE 4-8

a' AND b' FOR LONGITUDE AND TIME

TIME OF D_{st}(hr)	LONGITUDE												ALL LONGITUDES	
	0° - 60°E		60°-120°E		120°-180°E		180°-240°E		240°-300°E		300°-360°E			
	a'	b'	a'	b'	a'	b'	a'	b'	a'	b'	a'	b'	a'	b'
t	6.60	-.0246	6.74	.0009	6.17	-.0222	5.66	-.0383	5.46	-.0388	6.94	-.0179	6.37	-.0239
t-1	6.64	-.0250	6.78	.0028	6.10	-.0228	5.61	-.0414	5.75	-.0317	6.98	-.0186	6.42	-.0227
t-2	6.77	-.0187	6.76	.0015	5.99	-.0223	5.67	-.0391	6.39	-.0164	7.05	-.0187	6.50	-.0198
t-3	6.74	-.0178	6.76	.0018	5.88	-.0238	5.50	-.0448	6.62	-.0110	7.22	-.0111	6.58	-.0166
t-4	6.63	-.0217	6.74	.0007	5.82	-.0237	5.96	-.0358	6.64	-.0114	7.21	-.0132	6.62	-.0148
t-5	6.61	-.0199	6.74	.0006	5.82	-.0254	6.54	-.0168	6.52	-.0171	7.26	-.0092	6.69	-.0114
t-6	6.70	-.0169	6.70	-.0009	5.96	-.0217	6.49	-.0186	6.47	-.0210	7.29	-.0064	6.73	-.0102
t-7	6.60	-.0176	6.69	-.0011	6.06	-.0173	6.83	-.0058	6.62	-.0173	7.23	-.0102	6.74	-.0093
t-8	6.60	-.0158	6.67	-.0017	5.93	-.0194	7.01	.0032	6.77	-.0111	7.23	-.0098	6.75	-.0088
t-9	6.51	-.0166	6.69	-.0013	6.30	-.0098	7.03	.0055	6.74	-.0151	7.28	-.0055	6.77	-.0080
t-10	6.45	-.0162	6.71	-.0006	6.60	-.0012	7.02	.0074	6.76	-.0124	7.23	-.0080	6.77	-.0078
t-11	6.38	-.0185	6.70	-.0009	6.63	-.0001	6.83	-.0112	6.85	-.0063	7.23	-.0077	6.76	-.0086
t-12	6.39	-.0171	6.76	.0010	6.58	-.0022	6.87	-.0122	6.79	-.0094	7.18	-.0092	6.74	-.0094

Table 4-9 presents the S_ρ corresponding to Table 4-8. The correlation between density and D_{st} is good only at certain longitudes and delay times, as indicated by large values of the average/minimum S_ρ ratios at the bottom of the table in the 120°E to 180°E and 180°E to 240°E sectors with time delays of 4 hr and 0 hr, respectively. The standard error is low at 16.5 percent for D_{st} from t to t-12 hr in the 60°E to 120°E sector. For some reason, there is little or no correlation between density and D_{st} in this sector. The same is true for density and a_p (Table 4-5). Since changes in D_{st} do not result in appreciable changes in density, the scatter of points in the scatter diagram is less, resulting in low standard error. The relative density values at the bottom of Table 4-9 indicate that there is not much variation of density with longitude as pointed out before.

4.2.4 Discussion

Table 4-10 gives a comparison between the standard error resulting using a_p (Table 4-3) and D_{st} (Table 4-7) for geomagnetic latitude and delay times of 0, 3, 6, 9, and 12 hr. In all cases, the standard error is lower using a_p than D_{st}, averaging 19.3 percent lower. Also, the average/minimum S_ρ ratios are appreciably higher for a_p than D_{st} at 0°N, 10°N, and 20°N. For these latitudes, the minimum standard error for a_p occurs at t-3 hr, where it averages 37.8 percent lower than that for D_{st} at the same time delay. Therefore, it appears that the density can be predicted best at low latitudes using a_p at t-3 hr, at least during the period under consideration.

Table 4-11 shows a comparison between standard errors resulting from using a_p (Table 4-5) and D_{st} (Table 4-9) for 60-degree longitude sectors and all longitudes (0° - 360°E) for delay times 0, 3, 6, 9, and 12 hr. In all longitude sectors the average standard error is lower using a_p than D_{st}, averaging 21.2 percent lower. Based on the average/minimum S_ρ ratio only, a_p is clearly superior to D_{st} for predictive purposes in the 0° to 60°E and 300° to 360°E sector with time delays of 3 and 6 hr, repectively. D_{st} appears better at 120° -

TABLE 4-9

D_{St}, STANDARD ERROR FOR LONGITUDE AND TIME

TIME OF D_{St} (hr)	LONGITUDE						ALL LONGITUDES
	0°-60°E	60°-120°E	120°-180°E	180°-240°E	240°-300°E	300°-360°E	
t	24.6	16.5	18.2	18.7*	19.8*	25.3*	22.7*
t-1	24.5	16.5	17.2	19.2	21.1	25.5	23.2
t-2	25.6	16.5	15.8	21.1	23.2	25.5	23.6
t-3	25.5	16.5	15.2	24.0	23.4	26.0	24.3
t-4	24.9	16.5	15.1*	29.9	23.4	25.9	24.7
t-5	24.9	16.5	17.0	32.8	22.7	26.1	25.3
t-6	25.5	16.5	19.3	32.5	22.6	26.3	25.4
t-7	24.9	16.5	20.3	33.3	23.2	26.1	25.4
t-8	24.9	16.5	20.0	33.3	23.4	26.1	25.6
t-9	24.5	16.5	21.4	33.3	23.2	26.3	25.6
t-10	24.1	16.5	21.8	33.3	23.4	26.1	25.6
t-11	23.6*	16.5	21.8	33.2	23.9	26.1	25.4
t-12	24.1	16.5	21.5	33.0	23.6	26.0	25.4
AVE.	24.7	16.5	18.8	29.0	22.8	25.9	24.8
AVE./MIN	1.08	1.00	1.44	1.78	1.21	1.04	1.09
n	65	50	55	49	45	64	328
REL. DENSITY	1.02	.97	.96	1.00	.99	1.06	1.00

*Minimum.

TABLE 4-10

a_p AND D_{St}, STANDARD ERROR FOR LATITUDE AND TIME

TIME OF a_p AND D_{St} (hr)	GEOMAGNETIC LATITUDE										ALL LATITUDES	
	0° N		10° N		20° N		30° N		40° N			
	a_p	D_{St}	a_p	D_{St}	a_p	D_{St}	a_p	D_{St}	a_p	D_{St}	a_p	D_{St}
t	15.7	21.1*	21.5	24.3*	21.1	23.6*	18.9	22.6*	13.9	14.8*	20.3	22.7*
t-3	14.1*	23.0	16.0*	25.1	15.5*	25.2	19.4	23.8	13.9	15.6	17.5*	24.3
t-6	19.3	24.5	20.3	26.3	16.7	26.2	18.4	24.0	14.4	16.3	19.1	25.4
t-9	22.2	25.1	24.5	26.6	19.8	26.5	18.0*	24.0	13.2*	16.1	21.0	25.6
t-12	21.6	25.0	24.6	26.4	20.6	26.4	20.0	24.0	15.3	16.1	21.8	25.4
AVE.	18.6	23.7	21.4	25.7	18.7	25.6	18.9	23.7	14.1	15.8	19.9	24.7
AVE./MIN	1.32	1.12	1.34	1.06	1.21	1.08	1.05	1.05	1.07	1.07	1.14	1.09
n	49	49	80	80	89	89	80	80	30	30	328	328

*Minimum.

TABLE 4-11

a_p AND D_{St}, STANDARD ERROR FOR LONGITUDE AND TIME

TIME OF a_p AND D_{St} (hr)	LONGITUDE												ALL LONGITUDES	
	0°-60°E		60°-120°E		120°-180°E		180°-240°E		240°-300°E		300°-360°E			
	a_p	D_{St}	a_p	D_{St}	a_p	D_{St}	a_p	D_{St}	a_p	D_{St}	a_p	D_{St}	a_p	D_{St}
t	19.6	24.6	14.5*	16.5	13.0*	18.2	21.7	18.7*	20.4	19.8*	20.7	25.3*	20.3	22.7*
t-3	15.8*	25.5	15.7	16.5	14.0	15.2*	13.5*	24.0	17.6*	23.4	19.3	26.0	17.5*	24.3
t-6	17.2	25.5	17.0	16.5	13.1	19.3	14.5	32.5	18.8	22.6	16.2*	26.3	19.1	25.4
t-9	22.0	24.5	17.2	16.5	14.5	21.4	20.3	33.3	17.6	23.2	18.8	26.3	21.0	25.6
t-12	22.3	24.1*	14.6	16.5	15.4	21.8	26.6	33.0	18.5	23.6	22.7	26.0	21.8	25.4
AVE.	19.4	24.8	15.8	16.5	14.0	19.2	19.3	28.3	18.6	22.5	19.5	26.0	19.9	24.7
AVE./MIN	1.23	1.03	1.09	1.00	1.08	1.26	1.43	1.51	1.06	1.14	1.21	1.03	1.14	1.09
n	65	65	50	50	55	55	49	49	45	45	64	64	328	328

*Minimum.

180°E at t-3 hr. The high value of both average/minimum S_ρ ratios in the 180° - 240°E sector indicates that the density is well correlated in this sector indicates that the density is well correlated in this sector with both a_p and D_{st}, with time delays of 3 and 0 hr, respectively. The low values of both ratios in the 60° to 120°E and 240° to 300°E sectors indicates that density is poorly correlated with both a_p and D_{st}. In these sectors it seems preferable to use a_p since it results in a lower standard error.

In Table 4-3 the minimum standard error occurs for a_p at t-3 hr at 0°N, 10°N, and 20°N. No significance is attached to the fact that the minimum $S\rho$ occurs at t-9 hr at 30° and 40°N because the average/minimum $S\rho$ ratios are low for these latitudes. The density at 0° - 20°N may correlate best with the a_p value 3 hr earlier because there is a time delay of about 3 hr between the peak geomagnetic activity in the auroral zone and the atmospheric response at low latitudes. If the main atmospheric heating is caused by some mechanism or energy source in the auroral regions, then wave propogation transport the energy from the auroral region to the equatorial region within a time interval of about 3 hr. Jacchia and Slowey (1967), from satellite-drag analysis, give a mean time delay of 7.2 ± 0.3 hr for an average latitude of 25 degrees. However, the inaccuracies associated with satellite-drag measurements have been discussed already (also, see Taeusch et al., 1971).

DeVries (1971), reporting on neutral density data obtained from the Low-G Calibration System (LOGACS) flown on a polar orbiting satellite during a period of high geomagnetic activity (May 22-26, 1967), states that the in-situ high resolution data show that the density increases almost simultaneously with enhanced geomagnetic activity. The largest density increases occurred in the region of the maximum current of the auroral electrojet with no significant increases in the equatorial region until several hours later. Atmospheric waves, apparently

associated with joule heating, appear to originate in the auroral region at altitudes lower than 150 km and propagate upward toward the Equator. Blamont and Luton (1970) analyzed thermospheric measurements from data obtained by a Fabry-Perot interferometer on OGO-6 in the period 26 September - 6 October 1969, during which two large geomagnetic disturbances occurred. These temperature measurements showed a 300°K increase in the two polar regions while the temperature near the Equator increased by only 90°K.

Volland and Mayr (1971) calculated the response of thermospheric density during geomagnetic disturbance, assuming that an impulse type of heat input is injected into a small band of latitude within the auroral oval during local nighttime. They calculated the temporal response of the thermospheric density to the heat input. This theory indicates a dependence of the atmospheric density changes on latitude and longitude. The general trend of the density variations is in agreement with the trend observed in the LOGACS observations (DeVries, 1971). The data in Table 4-5 indicate that there is a good correlation between density and a_p at t-3 hr at 180° to 240°E and little or no correlation at 60° to 120°E and 240° to 300°E. Table 4-9 indicates correlation between density and D_{st} between 180° to 240°E with no time delay and little or no correlation between 60° to 120°E.

May and Miller (1971) have shown from a rather limited sample of satellite spin-rate data that the variations in density at 310 km in low latitudes are more closely indicated by Equatorial D_{st}, with a 2-hr lag of density behind D_{st}, than by a_p with the 7-hr lag suggested by Jacchia and Slowey (1967). The improvement of the relationship with D_{st} as compared with a_p is most marked in the recovery phase following the peaks of magnetic storms. At these times the density recovers more slowly than a_p, in common with D_{st}. May and Miller state that it is not possible with their data to test whether or not the improvement was caused by the density being measured in low latitudes, where the

magnetic observations from which Equatorial D_{st} is evaluated are made. The minimum S_ρ values in Table 4-7 indicate no lag in time between density and D_{st}, except at 10°N, where it is 2 hr. According to DeVries (1971), the density increases simultaneously with a_p in auroral latitudes, near where a_p is measured. If this is true, it appears reasonable to expect that likewise no lag should occur between the density and D_{st} at low latitudes, where D_{st} is measured, provided that the geomagnetic disturbance causes worldwide heating simultaneously. The 3-hr lag between the density at low latitudes and a_p (Table 4-3) could result from the fact that most of the energy is initially deposited in auroral latitudes and later transported southwards by wave or bulk mass motion.

4.3 References

Anderson, A. D.; Existance of a significant latitudinal variation in density from 200 to 800 kilometers, Nature, 209, 656, 1966.

Anderson, A. D.; A model for the semi-annual effect appearing in the drag data of satellites in eccentric orbits, Lockheed Missiles and Space Co. Report, LMSC 6-78-69-37 (N70-23721), 1969.

Anderson, A. D. and G. W. Sharp; Neutral density measurements near 400 kilometers by a microphone density gage on OGO-6 during 12-15 July 1969, J. Geophs. Res., 77, 1878, 1972.

Chandra, S., E. J. Maier, B. E. Troy and B. C. Narasinga Rao, The sub-auroral red arc and the associated ionospheric phenomena, NASA Tech. Rept. TM X - 65307, Greenbelt, Maryland, 1970.

Chappell, C. R., K K. Harris and G. W. Sharp, OGO-5 measurement of the plasmasphere during observations of stable auroral red arcs, J. Geophys. Res., 76, 2357, 1971.

Cole, K. D., Stable auroral red arcs, sinks for energy of D_{st} main phase, J. Geophys. Res., 70, 1689, 1965.

Dalgarno, A., Corpuscular radiation in the upper atmosphere, Ann. Geophys., 20, 65, 1964.

DeVries, L. L.; Structure and motion of the thermosphere shown by density data from the low-G accelerometer calibration system (LOGACS), URSI/COSPAR Meeting, June 24-26, 1971, Seattle, Washington 1971.

Hedin, A. E. and H. G. Mayr; Magnetic control of neutral thermospheric density near the equator, Trans. Amer. Geophys. Union, 52, 872, 1971.

Hess, W. N.; Introduction to Space Science, Gorden and Breach Science Publishers, New York, 1965.

Hoch, R. J., and K. C. Clark, Recent occurrences of stable auroral red arcs, J. Geophys. Res., 75, 2511, 1970.

Hoch, R. J., and L. L. Smith, Location in the magnetosphere of field lines leading to SAR arcs, J. Geophys. Res., 76, 3079, 1971

Jacchia, L. G. and J. Slowey; Geomagnetic perturbations and upper-atmosphere heating, J. Geophys. Res., 72, 1423, 1967.

King, G. A. M., and F. E. Roach, Relationship between red auroral arcs and ionospheric recombination, J. Res. N.B.S., 65D, 129, 1961.

May, B. R. and D. E. Miller; The correlation between air density and magnetic disturbance decued from changes of satellite spin-rate, Planet. Space Sci., 19, 39, 1971.

Megill, L. R., and T. Van Zandt, Heating of the neutral atmosphere during magnetic storms, Trans AGU, 45, 355, 1964.

Newton, G. P., R. Horowitz and W. Priester, Atmospheric density and temperature variations from the Explorer XVII satellite and a further comparison with satellite drag, Planet. Space Sci., 13, 599, 1965.

Newton, G. P. and D. T. Pelz; Latitudinal variations in the neutral atmospheric density, J. Geophys. Res., 74, 4169, 1969.

Norton, R. B., and J. A. Findlay, Electron density and temperature in the vicinity of the 29 September 1967 middle latitude red arc, Planet, Space Sci., 17, 1867, 1969.

Nurre, G. S. and L. L. DeVries; An experiment to determine density variations in the earth's atmosphere and other atmospheric and aerodynamic information, Fourth National Conference on Aerospace Meteorology, May 4-7, 1970, Las Vegas, Nevada, 1970.

Reber, C. A., D. N. Harpold, R. Horowitz and A. E. Hedin; Horizontal distribution of helium in the earth's upper atmosphere, J. Geophys. Res., 76, 1845, 1971.

Rees, M. H., Excitation of high-altitude red auroral arcs, Planet. Space Sci., 8, 59, 1961.

Roach, F. E., and J. R. Roach, Stable 6300A auroral arcs in mid-latitudes, Planet. Space Sci., 11, 523, 1963.

Roble, R. G., A theoretical and experimental study of the stable mid-latitude red arc (SAR arc), Ph.D. Thesis, University of Michigan, Ann Arbor, Michigan, 1969.

Roble, R. G., and R. E. Dickinson, Atmospheric response to heating within a stable auroral red arc, Planet. Space Sci., 18, 1489, 1970.

Roble, R. G., P. B. Hays and A. F. Nagy, Photometric and interferometric observations of a mid-latitude stable auroral red arc, Planet. Space Sci., 18, 431, 1970

Siguira, M. and S. J. Cain; Provisional hourly values of Equatorial Dst for 1964, 1965, 1966 and 1967, NASA Goddard Space Flight Center Rept. X-612-69-20 (N69-20074), 1969.

Taeusch, D. R., G. R. Carignan, and C. A. Reber; Response of the neutral atmosphere to geomagnetic disturbances, Space Res., 9, 995, 1971.

U. S. Space Science Board, Physics of the Earth in Space, National Research Council, National Academy of Sciences, 1968.

Volland, H. and H. G. Mayr; Response of the thermospheric density to auroral heating during geomagnetic disturbances, J. Geophys. Res. 76, 3764, 1971.

Walker, J. C. G., and M. H. Rees, Excitation of stable auroral red arcs at sub-auroral latitudes, Planet. Space Sci., 16, 915, 1968.

Chapter 5

CONCLUSIONS

Chapter 5

CONCLUSIONS

5.1 Conclusions

Although the Microphone Density Gage did not operate in flight quite as it was expected to do (that is, significant loss in sensitivity was experienced), some reasonably useful scientific information has resulted from the analysis of the data that was obtained.

If it is true that the density peaks and SAR arcs result from the same heating mechanism as discussed in Chapter 4, then the microphone density gage is a new, powerful instrument for detecting and measuring the extent, intensity and other characteristics of SAR arcs. Although absolute accuracy of the microphone density gage is uncertain, the present analysis indicates that the density gage measures relative density variations accurately. The density peak characteristics are largely independent of the absolute accuracy of the microphone gage and are influenced primarily by the relative precision of the gage measurements, which is believed to be better than 95 percent. Rather precise changes in SAR arcs can be derived from measurements of the microphone density gage. The temperature changes in SAR arcs derived from measurements with Fabry-Perot interferometers are limited in precision to $\pm$ 75°K for ground-based instrument (Roble, 1969) and $\pm$ 50°K for instruments on satellites (Blamont and Luton, 1970). In addition, the density gage offers a marked advantage over both types of interferometers in that it can make measurements of SAR arcs during the daytime. It is not limited by daylight, moonlight, or clouds.

Analysis of the Microphone Density Gage data shows that marked density increases occur at low latitudes during geomagnetic storms. The average density from 10°N to 20°N is over twice as great for K_p = 8 as K_p = 0. The best least-squares fit and corresponding delay time

between density and a magnetic index can be determined for a given latitude or longitude sector from the minimum standard error. The average/minimum standard error ratio indicates whether or not there is a good correlation between the density and the magnetic index having the time delay associated with the minimum standard error. Large average/minimum standard error ratios occur at 0^{o}N, 10^{o}N, and 30^{o}N geomagnetic latitude where the minimum standard error occurs for a_p at t-3 hr. The average/minimum ratio is very large in the longitude sector 180^{o} to 240^{o}E, where the minimum standard error occurs at a time delay of 3 hr between density and a_p.

With regard to density and D_{st}, the best correlation at low latitudes results with no time delay, except at 10^{o}N, where it is 2 hr. Like a_p, the best correlation with longitude occurs at 180^{o} to 240^{o}E. In most cases, the correlation of density with D_{st} is not as good as that with a_p, as indicated by the magnitudes of the standard errors and average/minimum ratios. It appears that the density can be predicted best at low latitudes using a_p at t-3 hr. If the minimum values of the standard error reflect the time delay between the onset of a storm (as indicated by a_p and D_{st}), then inasmuch as there is little or no lag between density and D_{st} and about a 3 hr lag between density and a_p, this indicates that a geomagnetic disturbance causes worldwide heating simultaneously, with most of the heating ensuing in the auroral zones, some of which is later transported to low latitudes.

Chapter 6

NEW TECHNOLOGY

Chapter 6

NEW TECHNOLOGY

6.1 New Technology

The fundamental principles and procedures utilized in the Ribbon Microphone Density Gage were developed prior to the awarding of this contract. Therefore, no New Technology was developed under this contract effort.